Title: The effect of clinically-controllable factors on neural activation during dorsal root ganglion stimulation

Robert D. Graham, MSE[1,2], Tim M. Bruns, PhD[1,2], Bo Duan, PhD[3], and Scott F. Lempka, PhD[1,2,4,*]
[1]Department of Biomedical Engineering, [2]Biointerfaces Institute, [3]Department of Molecular, Cellular, and Developmental Biology, [4]Department of Anesthesiology, University of Michigan, Ann Arbor, MI 48109, United States
[*]lempka@umich.edu

Corresponding Author:
Scott F. Lempka, PhD
Department of Biomedical Engineering
University of Michigan
2800 Plymouth Road, NCRC 014-184
Ann Arbor, MI 48109-2800
Email: lempka@umich.edu

Abstract

Objective: Dorsal root ganglion stimulation (DRGS) is an effective therapy for chronic pain, though its mechanisms of action are unknown. Currently, we do not understand how clinically-controllable parameters (e.g. electrode position, stimulus pulse width) affect the direct neural response to DRGS. Therefore, the goal of this study was to utilize a computational modeling approach to characterize how varying clinically-controllable parameters changed neural activation profiles during DRGS.

Methods: We coupled a finite element model of a human L5 dorsal root ganglion to multi-compartment models of primary sensory neurons (i.e. Aα-, Aβ-, Aδ-, and C-neurons). We calculated the stimulation amplitudes necessary to elicit one or more action potentials in each neuron, and examined how neural activation profiles were affected by varying clinically-controllable parameters.

Results: In general, DRGS predominantly activated large myelinated Aα- and Aβ-neurons. Shifting the electrode more than 2 mm away from the ganglion abolished most DRGS-induced neural activation. Increasing the stimulus pulse width to 500 μs or greater increased the number of activated Aδ-neurons, while shorter pulse widths typically only activated Aα- and Aβ-neurons. Placing a cathode near a nerve root, or an anode near the ganglion body, maximized Aβ-mechanoreceptor activation. Guarded active contact configurations did not activate more Aβ-mechanoreceptors than conventional bipolar configurations.

Conclusions: Our results suggest that DRGS applied with stimulation parameters within typical clinical ranges predominantly activates Aβ-mechanoreceptors. In general, varying clinically-controllable parameters affects the number of Aβ-mechanoreceptors activated, although longer pulse widths can increase Aδ-neuron activation. Our data support several Neuromodulation Appropriateness Consensus Committee guidelines on the clinical implementation of DRGS.

Keywords: Dorsal root ganglion; electric stimulation; chronic pain; computer simulation; spinal cord stimulation; dorsal roots;

Conflict of Interest: Scott F. Lempka holds stock options, has received research support, and serves on the scientific advisory board of Presidio Medical, Inc., and is a shareholder in Hologram Consultants, LLC. All other authors declare no conflicts of interest.

Introduction

Chronic pain poses one of the greatest public health challenges currently facing the United States, with more than 14 million Americans reporting they live with “a lot of pain” on a daily basis (1). In an effort to combat the pain epidemic, the prescription rate of opioids, a common pharmacological pain management strategy, quadrupled over the past 20 years (2). Over the same timeframe, there was a 200% increase in the rate of overdose deaths involving opioids (3). As the death rates from opioid-related drug overdoses have continued to climb in recent years (4), the need for non-addictive pain therapies has become even more pressing.

Neurostimulation therapies are effective, non-addictive treatment strategies for chronic pain that is refractory to conventional medical management. Spinal cord stimulation (SCS) is a neurostimulation therapy primarily used to treat intractable neuropathic pain in the lower limbs (e.g. failed back surgery syndrome) (5). SCS is achieved by implanting an electrode lead in the spinal epidural space, and applying brief electrical impulses to the dorsal columns (6). However, due to the complex anatomy of the spinal column, SCS struggles to treat certain pain etiologies, particularly pain that is highly focalized to specific dermatomes (i.e. regions of the body), such as the groin and foot (7).

Dorsal root ganglion stimulation (DRGS) was approved by the United States Food and Drug Administration in early 2016 for the treatment of intractable complex regional pain syndrome in the lower limbs (8, 9), and has shown success at treating several other focal pain indications (e.g. phantom limb pain, painful diabetic neuropathy, groin pain) (10–12). In contrast to SCS, DRGS electrodes are placed in the intraforaminal space, where they apply electrical stimulation to a single dorsal root ganglion (DRG). There are bilateral pairs of DRG at each level of the spinal cord, with each DRG containing the cell bodies, and a portion of the axons, of all the primary sensory neurons innervating a single dermatome (13). DRG neurons are pseudounipolar: a single axon process extends from the soma, bifurcates at a large node of Ranvier called the T-junction, and forms an axon that projects to the spinal cord and an axon that extends to the periphery (14). Due to the precise targeting of a single dermatome’s primary afferents, DRGS is rationalized to provide patients with focal, dermatome-specific pain relief.

Although preliminary clinical results indicate that DRGS provides adequate pain relief for many patients, approximately 20-30% of patients do not receive sufficient pain relief from DRGS (9). Furthermore, long-term studies showed that DRGS may lose efficacy over time (12, 15), a trend also found in long-term clinical studies of SCS (16, 17). These two shortcomings of DRGS can partially be attributed to the fact that we do not have a clear understanding of the physiologic mechanisms of action of DRGS. Uncovering the mechanisms by which DRGS provides pain relief will allow scientists and engineers to innovate the technology to specifically target these mechanisms to ultimately improve clinical outcomes.

A recent computational modeling study suggested that DRGS may provide pain relief by augmenting a low-pass filtering mechanism at the T-junction, preventing nociceptive impulses from propagating from the periphery to the spinal cord (18). However, the stimulation amplitudes necessary to augment T-junction filtering (> 9 mA) were far greater than the amplitudes used clinically (≤ 1 mA on average). Using a similar computational modeling approach, we recently showed that for stimulation parameters used clinically, DRGS may directly activate large-diameter myelinated Aβ low threshold mechanoreceptors (Aβ-LTMRs) (putative innocuous touch-sensing neurons), but not small-diameter nonmyelinated C-nociceptors (putative nociceptors) (19). However, this study did not examine the effect of DRGS on Aα-neurons, large myelinated afferents that innervate muscles (20), or Aδ-neurons, a diverse class of medium-diameter, thinly myelinated afferents that can convey noxious or innocuous sensations (21). Furthermore, there are several clinical factors which affect the delivery of electrical stimulation to neural tissue, such as the placement of the electrode lead relative to the neural target (19, 22, 23) and the choice of stimulation parameters (e.g. pulse width, pulse frequency) (24, 25). Currently, it remains largely unclear how these clinically-controllable parameters affect the recruitment of different types of primary afferents for pain relief during DRGS. It is vital to understand how factors under clinical control influence neural activation, as these factors likely directly influence the efficacy of DRGS. Therefore, these factors are key in ensuring positive patient outcomes.

In this work, we employed a computer model of DRGS to study how clinical factors, such as electrode position and stimulation parameter selection, affect primary afferent recruitment. We coupled a finite element model (FEM) of a human L5 DRG to multi-compartment models of primary sensory neurons to study how these clinically-controllable factors affected neural activation during DRGS. We considered our results in context with the recommendations of the Neuromodulation Appropriateness Consensus Committee (NACC) on best practices for DRGS (26).

Methods

Building upon our prior work (19), we developed a computer model of DRGS to investigate how clinically-controllable factors (e.g. electrode position, stimulus parameter selection) affect neural activation in the DRG. We coupled a finite element model (FEM) of a human L5 DRG to multi-compartment models of sensory neurons. We used the FEM to calculate the voltage distribution generated by DRGS, and applied these voltages to the multi-compartment models. We examined which types of neurons generated action potentials in response to DRGS, and how neural activation patterns changed as we varied electrode position and stimulation parameters (i.e. pulse width, pulse frequency, stimulus configuration).

Step 1: Calculate the voltage distribution generated by DRGS

We constructed an FEM of a human L5 DRG and its surrounding anatomy (e.g. intraforaminal tissue, foraminal bone) based on experimentally measured values (Table 1, Figure 1). We based the geometry of the model on imaging and cadaver studies of human DRG and foraminal tissues (27–30). We wanted to examine the effect of electrode lead position relative to the ganglia, and the effect of lead distance from the ganglia on primary afferent recruitment. Therefore, we used a larger measured value for foraminal height (17.1 mm) in this

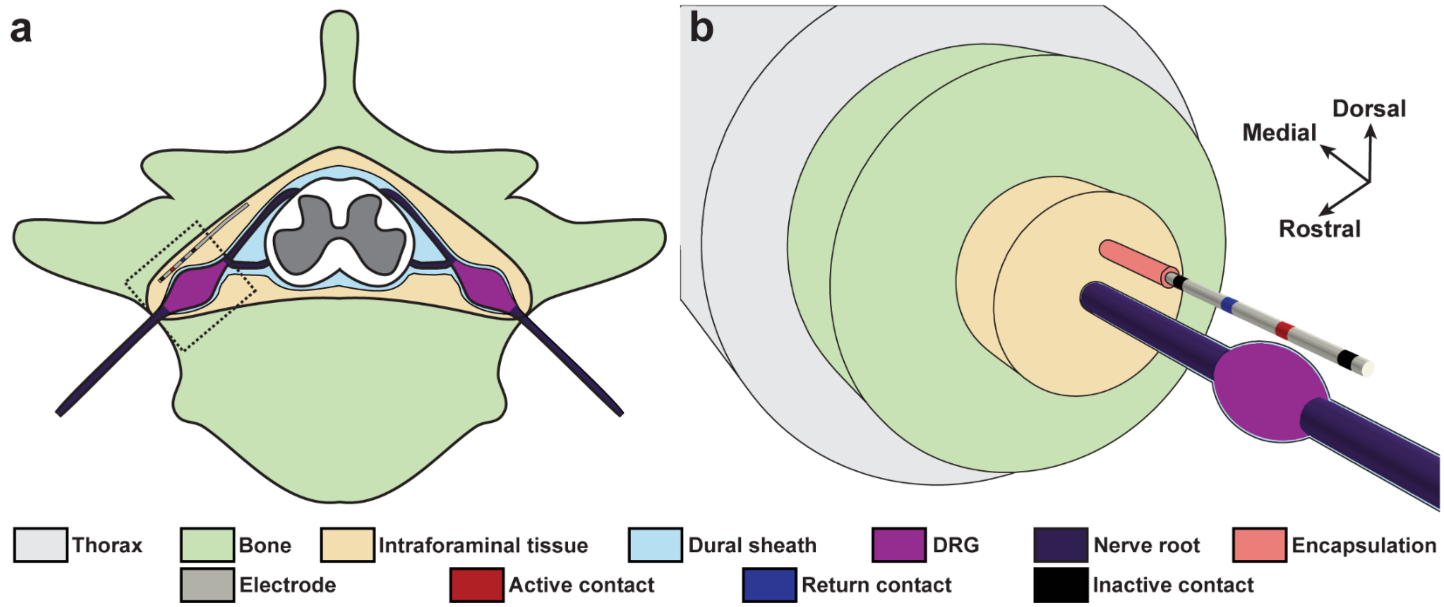

Figure 1: Finite element model (FEM) of a human L5 DRG and surrounding anatomy. a. Representative schematic of the human L5 spinal column, dorsal root ganglion, surrounding anatomy, and a four-contact DRGS electrode lead. The dashed box represents the general area represented by the FEM. b. Exploded view of the concentric cylindrical domains used to create the FEM. On the four-contact DRGS electrode lead, the red contact indicates the active contact, the blue contact is the return contact, and the black contacts are inactive.

model than in our previous model to allow a greater range of distances to be tested (27). We set the electrical conductivity of each tissue (Table 2) to the values used in our previous study of DRGS (19, 31–33). We modeled all conductivities as isotropic, with the exception of the nerve root, which we modeled as two-dimensionally (2D) anisotropic white matter (19). We built the FEM in the commercially-available software 3-matic Module within the Mimics Innovation Suite (Materialise, Belgium). We included an explicit representation of a four-contact DRGS electrode array in the FEM, with the second electrode contact centered above the middle of the DRG. In some simulations, we shifted the electrode 3.125 mm laterally along the nerve root axis, such that the midpoint between the second and third contacts was centered above the middle of the DRG (i.e. so the second and third contacts straddled the ganglion). We surrounded the electrode with a 300 μm encapsulation layer to represent the foreign body response to implanted materials (33).

We imported the FEM into COMSOL Multiphysics (COMSOL, Inc., USA). To simulate bipolar DRGS (26), we applied a unit current stimulation boundary condition (i.e. 1 A) to the active electrode contact and grounded (i.e. 0 V) the return contact. To improve stimulation selectivity, clinical SCS sometimes utilizes a guarded cathode stimulation configuration: two electrode contacts adjacent to the active contact are used as return contacts (34–36). To our knowledge, the use of a guarded cathode stimulation configuration in DRGS has not been reported. To explore the utility of the guarded cathode configuration in DRGS, we applied current stimulation to either the second or third contact, and grounded the contacts immediately adjacent to the active contact (e.g. grounding the first and third contacts for an active second contact). In all simulations, we modeled the electrode lead shaft as a perfect insulator, and inactive contacts as equipotential with zero net current across their surface. To calculate the voltage distribution generated by DRGS, we used the conjugate gradient method to solve Laplace's equation:

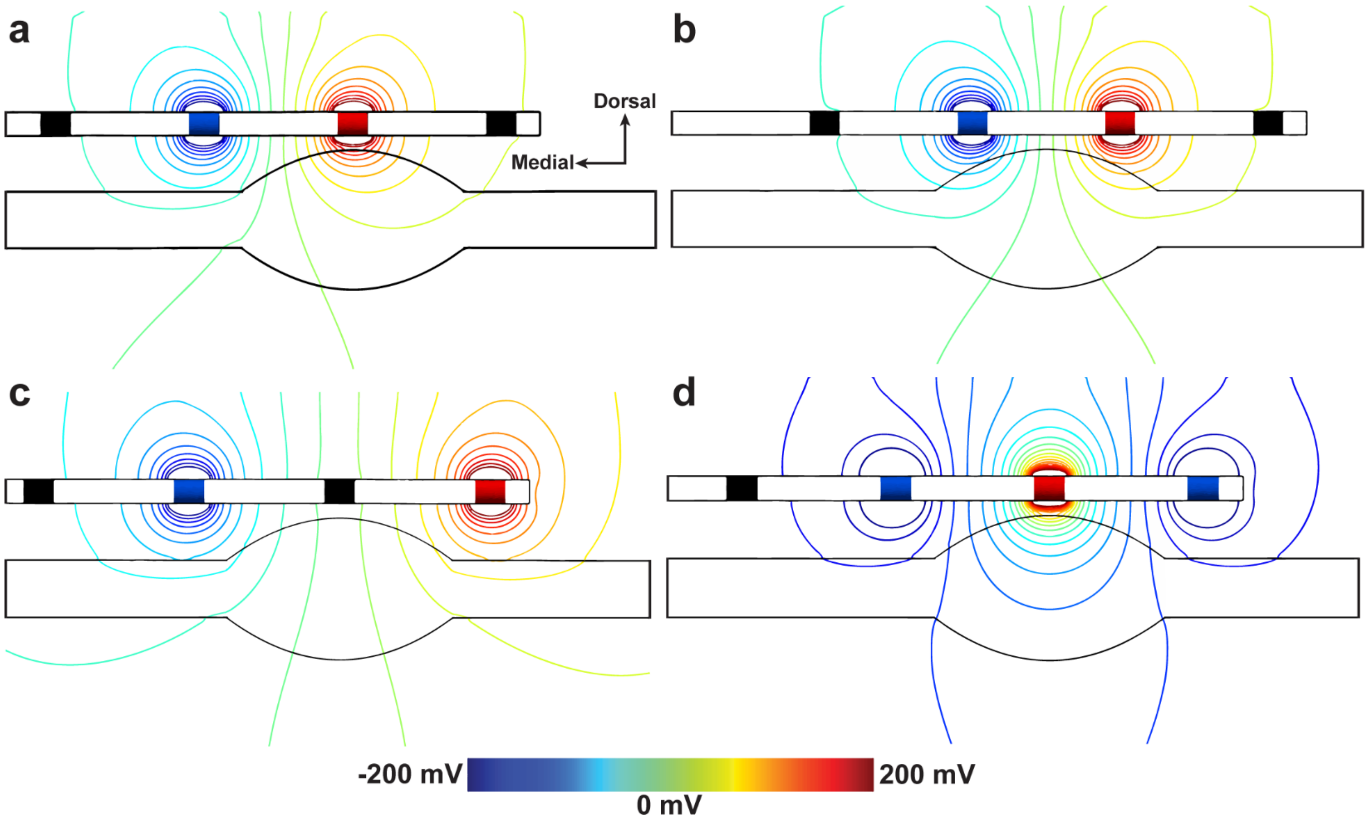

Figure 2: DRGS stimulation configurations. Isopotential lines of the voltage distributions generated by DRGS using example stimulation configurations: a. adjacent bipole with the active contact centered above the ganglion, b. adjacent bipole with the active and return contacts straddling the ganglion, c. separated bipole, and d. guarded cathode with the active contact centered above the ganglion. Red contacts are active contacts, blue contacts are return contacts, black contacts are inactive.

$$\nabla \cdot (\sigma \nabla \Phi) = 0 \ (1)$$

where σ is the tissue stiffness matrix, and Φ is the calculated voltage distribution. Figure 2 shows voltage distributions generated by DRGS using example stimulation configurations. We validated the FEM by its ability to produce bipolar impedances similar to impedances reported clinically (26). To calculate model impedance, we divided the average voltage across the active contact's surface by the applied stimulus current. From the ACCURATE clinical trial, average bipolar DRGS electrode impedances one year post-implant were 1458.9 ± 714.5 Ω (26). Our models produced a minimum bipolar impedance of 1357.55 Ω, when the active contact was centered immediately above the DRG and the return contact was adjacent to the active electrode and more proximal to the spinal cord. Our models produced a maximum bipolar impedance of 1551.54 Ω when the most distal contact and most proximal contact formed a longitudinal bipole pair. All model bipolar impedances fell within clinical range.

Step 2: Develop multi-compartment models of primary sensory neurons

We implemented multi-compartment models of primary sensory neurons found in human DRG using the NEURON simulation environment (v7.4) (37). We implemented previously-published models of an Aβ-LTMR and C-nociceptor (Figure 3a,d) (19). We developed a model of an Aα-afferent by extending the previously-published model of an Aβ-LTMR to include large-diameter (i.e. 15-16 μm) axons. Because Aα- and

Aβ-neurons share electrophysiological characteristics (38), we implemented the membrane dynamics of our previously-published Aβ-LTMR in our Aα-neuron model (Figure 3a). The Aα-neuron reproduced many action potential (AP) and conduction velocity (CV) data seen in experimental literature (e.g. AP height, duration) (Table 3). We developed two distinct multi-compartment models of Aδ-neurons: an LTMR (Figure 3b) and a high-threshold mechanoreceptor (HTMR) (Figure 3c) (21). Aδ-LTMRs and Aδ-HTMRs express distinct voltage-gated sodium channel profiles (39). Aδ-LTMRs mainly express Nav1.6, similar to other non-nociceptive myelinated mechanoreceptors (40), while Aδ-HTMRs express Nav1.7 and Nav1.8, similar to C-nociceptors (41, 42). Therefore, we developed two Aδ-neuron models, an LTMR and an HTMR model, distinguished by their active voltage-gated sodium channels. Both models had the same morphology. Each model had a soma 29 μm long and 34 μm wide, connected to a 3.0 μm stem axon (43). The Aδ-neuron axon morphologies (Table 4) were based on the MRG model of a mammalian peripheral axon (44). The stem axon extended 840 μm to match the total stem axon and soma length of the Aα-neuron, Aβ-LTMR, and C-nociceptor models (i.e. 869 μm), before splitting into two axons. One axon projected towards the spinal cord, with a diameter of 2.0 μm (43, 45), while the other projected to the periphery and had the same diameter as the stem axon (i.e. 3.0 μm) (43, 46). The original MRG axon model was parametrized for axons of specific diameters (e.g. 2.0, 5.7, 7.3 μm). To implement an axon with a diameter not included in the original model, such as the 3.0 μm stem and

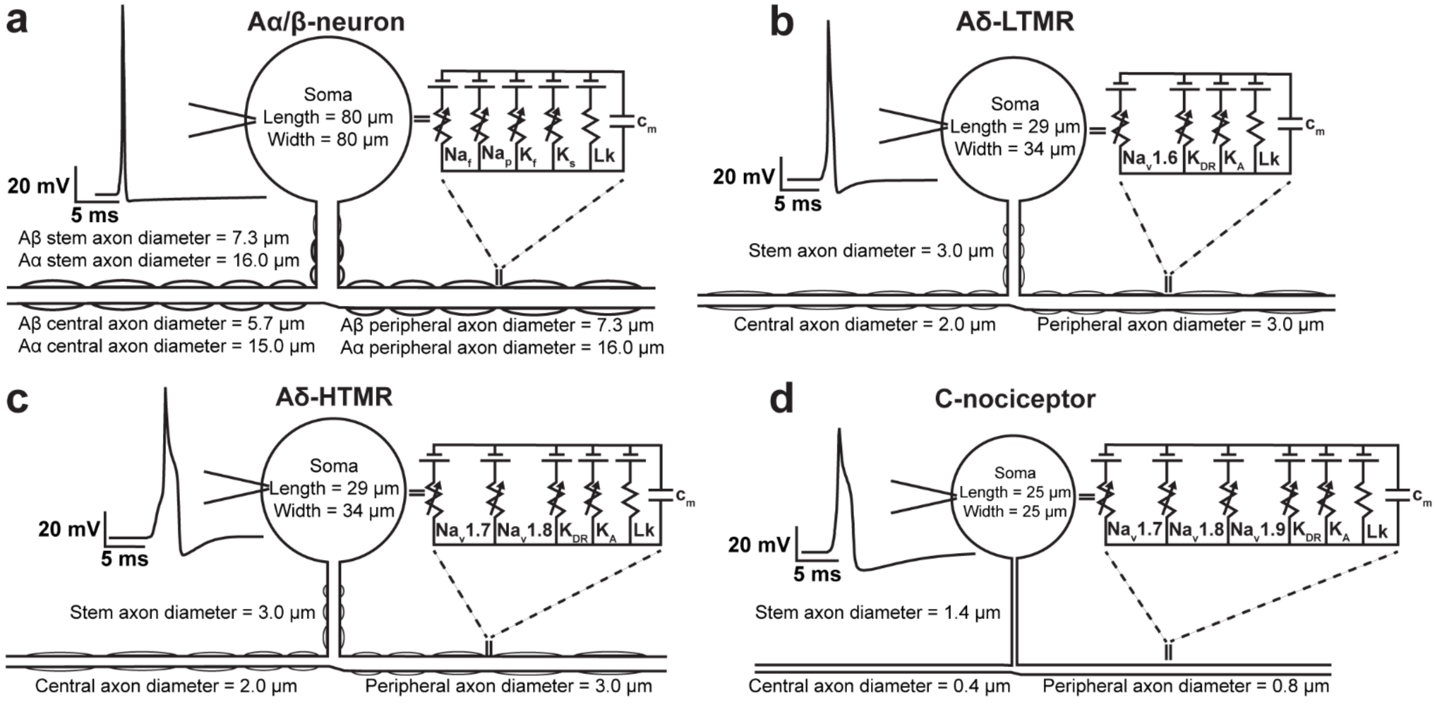

Figure 3: Multi-compartment models of DRG sensory neurons. We implemented models of five types of sensory neurons found in DRG: (a) a large-diameter, myelinated Aα- and Aβ-neurons; (b) a small-diameter, thinly-myelinated Aδ-LTMR; (c) a small-diameter, thinly-myelinated Aδ-HTMR; and (d) a small-diameter, nonmyelinated C-nociceptor. The Aα-neuron, Aβ-LTMR, and Aδ-LTMR putatively convey innocuous sensory information, while the Aδ-HTMR and C-nociceptor are putatively nociceptive. For each cell model, the equivalent circuit diagrams show the active voltage-gated ion channels included in each cell type and a linear leak conductance. Inset action potentials represent the somatic membrane response to a brief intracellular current pulse applied to the peripheral axon.

peripheral axons used in the Aδ-neuron models, we performed a linear regression to calculate the values of each parameter (e.g. number of myelin lamellae, internodal length) for a given axon diameter (47).

The nodes of Ranvier in the myelinated axon models were separated by three distinct finite impedance myelin segments: two myelin attachment sections, two paranode main segments, and six internodal segments (48). To reduce computational demand of the Aδ-neuron models (i.e. medium diameter myelinated axons with short internode distances), we modeled the internodal segments farther than 20 mm from the active electrode with only a single compartment. This simplification did not produce significant differences in the activation thresholds. The nodes of Ranvier contained active sodium and potassium conductances, and a linear leak conductance. Both models contained an A-type and delayed rectifier potassium conductance (49). The Aδ-LTMR model nodes contained a Nav1.6 conductance (50), while the Aδ-HTMR model nodes contained a Nav1.7 and Nav1.8 conductance (49). We set all nodal sodium conductances to 3.0 S/cm^2 (44). We set the LTMR model's somatic Nav1.6 conductance to 1.0 S/cm^2, to best reproduce electrophysiological data reported by literature. To best reproduce electrophysiological data, we set the HTMR model's somatic Nav1.8 conductance to 0.3 S/cm^2, A-type potassium conductance to 0.28 S/cm^2, delayed rectifier potassium conductance to 6 mS/cm^2, and all compartments' leak conductance to 2 mS/cm^2. We validated the models based on their ability to reproduce AP and CV data reported in literature (Table 5) (38, 51, 52).

Next, we distributed our multi-compartment models of primary afferent neurons throughout the DRG FEM as described previously (19). Previous histological studies of mammalian and human DRG showed that cell bodies preferentially organize around the dorsal edge of the ganglion (53, 54). Therefore, we generated two 2D regular grids – one intersecting the midpoint of the ganglion in the sagittal plane, and the other in the transverse plane – with 100 μm spacing in all directions, resulting in 2,304 points. We used each point on the grid as a seed point for the somata of the cell models described in Step 2. From each seed point, the stem axon projected towards the midline of the ganglion, then bifurcated into central and peripheral axon processes that curved ventrally to enter the nerve root (Figure 4a).

Step 3: Simulate the neural response to DRGS

We interpolated the extracellular potentials calculated in equation (1) onto the middle of each compartment of the cell models generated in Step 2. We applied the extracellular potentials to the multi-compartment models using NEURON's extracellular mechanism within the Python programming language (55). We calculated each compartment's time-varying membrane voltage in response to DRGS by using a backward Euler implicit integration method with a time step of 5 μs (Figure 4b). The tissue conductivities of the FEM were linear. Therefore, the voltage distribution generated by a specific DRGS amplitude was a scalar multiple of the voltage distribution generated by a unit stimulus (i.e. a 1 A stimulus) (56).

Our goal was to study how clinically-controllable factors (e.g. electrode lead position, stimulus parameters) affected neural activation in the DRG. Therefore, for each simulation, we calculated the minimum stimulus amplitude necessary to elicit one or more action potentials in each neuron type (i.e. the activation threshold). Each stimulus pulse was a charge-balanced, biphasic pulse with an active stimulus phase and a

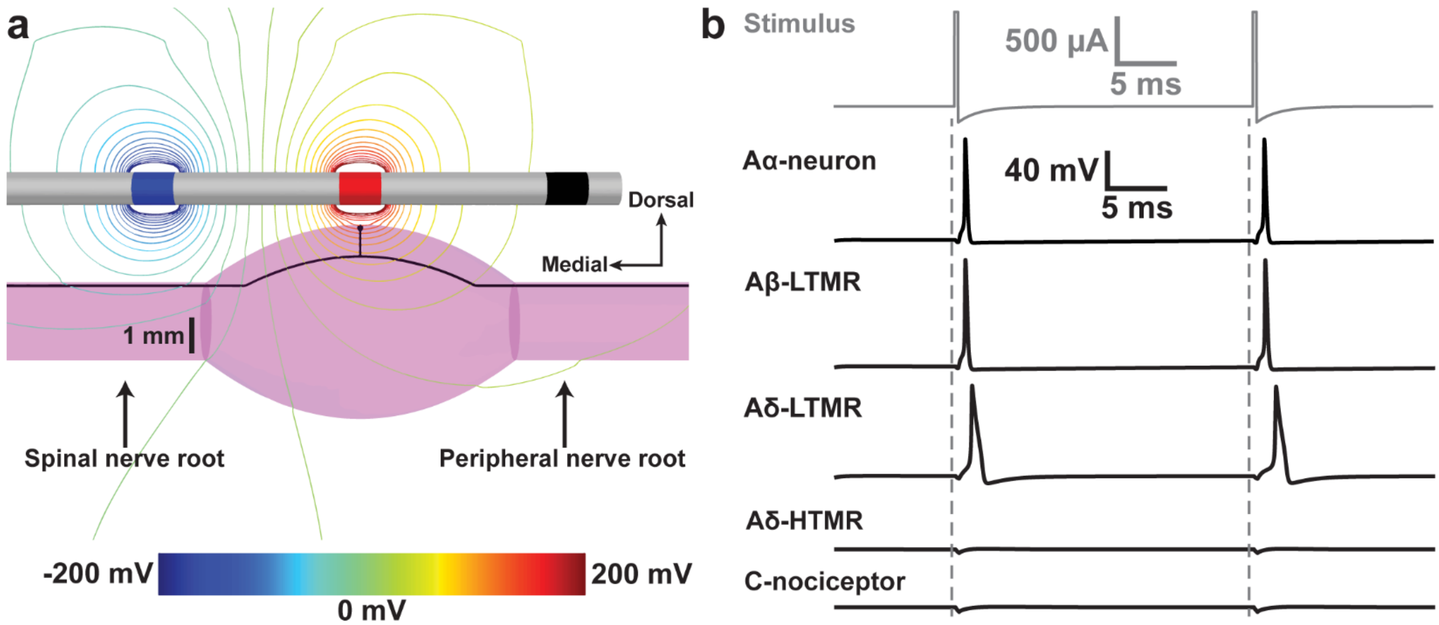

Figure 4: Simulating the neural response to DRGS. a. Isopotential lines of the voltage distribution generated by bipolar DRGS. The black trace in the DRG represents an example cell trajectory for a pseudounipolar primary sensory neuron. The red contact is the active contact, the blue contact is the return contact, and black contacts are inactive. b. Simulating the time-varying membrane potential of each sensory neuron cell type in response to a 1 mA anodic-first DRGS stimulus train (top trace, gray). The four black traces represent the somatic membrane potential of each type of sensory neuron with the example trajectory shown in part (a). Note that the putatively innocuous neurons (the Aα-neuron, Aβ-LTMR, and Aδ-LTMR) fire action potentials in response to a clinical DRGS pulse, while the putatively nociceptive models (the Aδ-HTMR and C-nociceptor) do not.

passive discharge phase with an interphase interval of 20 μs (18, 57). Unless otherwise noted, we calculated activation thresholds in response to a single stimulus pulse with a 300 μs active phase (the approximate average pulse width reported by the ACCURATE clinical trial (9)), with the electrode lead positioned directly above the ganglion (i.e. with a 0 mm electrode shift). We calculated activation thresholds for both anodic- and cathodic-first pulses (i.e. stimulus pulses with a positive active phase and negative active phase, respectively), using a binary search algorithm with a resolution of 0.1 μA.

We sought to identify which types of primary afferents (i.e. Aα-neurons, Aβ-LTMRs, Aδ-neurons, C-nociceptors) are likely activated by DRGS within parameter ranges used clinically. Therefore, we defined a maximum clinical amplitude of 2.0 mA, which is approximately the mean DRGS amplitude plus two standard deviations at one-year post implant reported by the ACCURATE clinical study (26). We considered any neuron with an activation threshold less than or equal to this maximum clinical amplitude (i.e. 2 mA) as activated within clinical ranges of stimulation parameters (i.e. clinical DRGS). When examining the effect of stimulus pulse frequency, we simulated 200 ms of DRGS with a pulse amplitude of 1 mA, and a pulse width of 300 μs. Then, we calculated the response frequency, i.e. the frequency of action potentials generated in response to DRGS of different pulse frequencies, of different types of neural compartments (e.g. the soma, the spinally-projecting axon, etc.).

Results

Effect of electrode position

Recent clinical studies have highlighted the importance of the electrode location relative to the ganglion to DRGS-induced pain relief (58, 59). To examine the effect of electrode position on DRGS-induced neural activation, we calculated activation thresholds for each cell type in response to DRGS applied with several electrode locations relative to the ganglion. Figure 5 shows the percentage of modeled neurons with activation

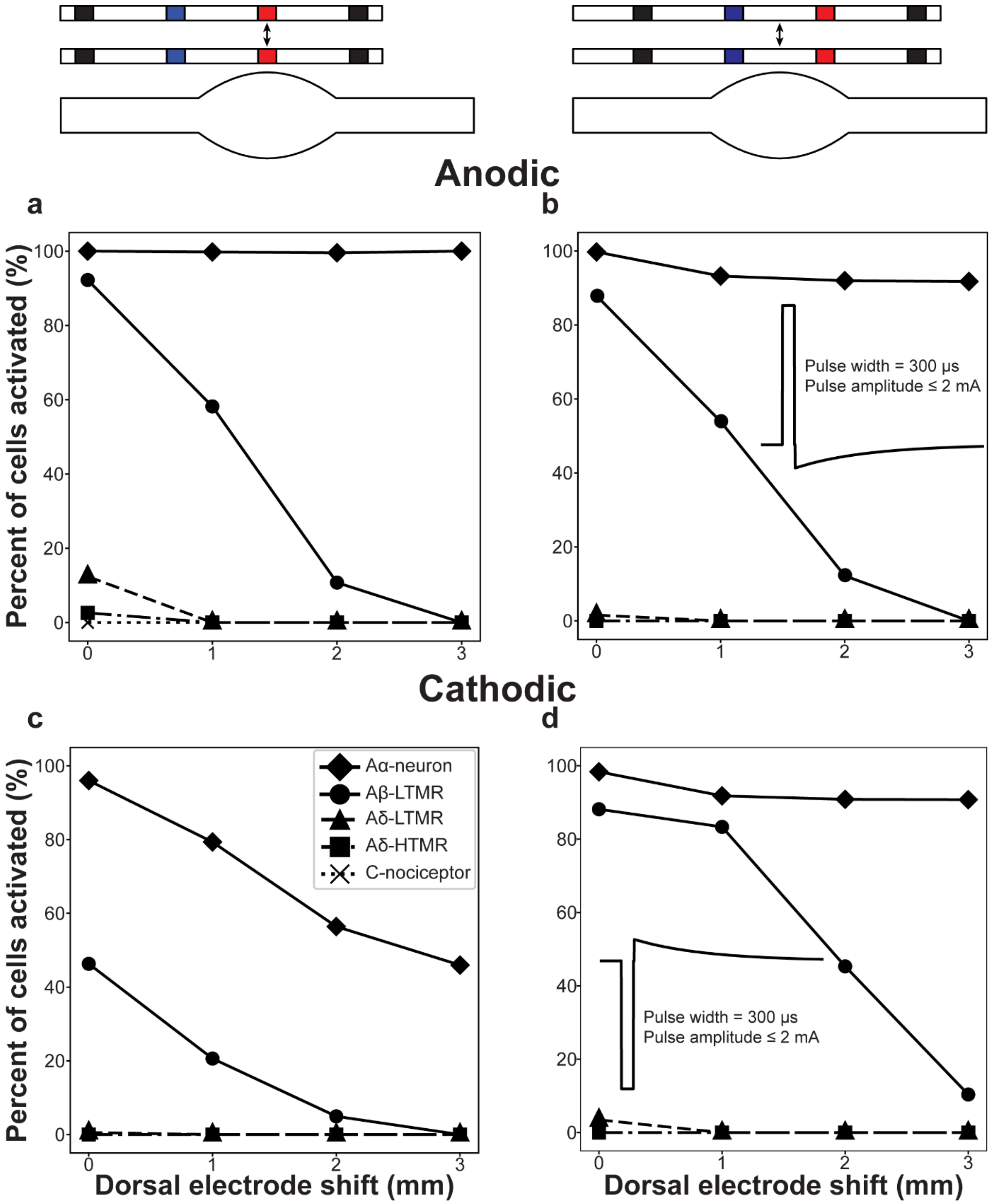

Figure 5: Effect of electrode position on neural activation during DRGS. Each plot shows the percentage of each neuron type that generated action potentials in response to DRGS with a pulse width of 300 μs and an amplitude 2 mA or less (i.e. clinical DRGS), as the distance between the electrode lead and the ganglion increased. We examined the effects of electrode position relative to the ganglion for several electrode positions and stimulus polarities: the active (red) contact centered above the ganglion (a, c), the active and return (blue) contacts straddling the ganglion (b, d), anodic-first DRGS (a, b), and cathodic-first DRGS (c, d).

thresholds within clinical range (i.e. ≤ 2 mA) as distance between the lead and the DRG increased, both when the active electrode contact was centered above the ganglion and when the active and return contacts straddled the ganglion.

In general, for all electrode lead positions, clinical DRGS only activated myelinated afferents (i.e. Aα-, Aβ- and Aδ-neurons) and did not activate nonmyelinated C-nociceptors (Figure 5). As the distance between the active contact and the ganglion increased, the percentage of myelinated afferents activated by clinical DRGS decreased. Generally, straddling the active and return contacts across the ganglion activated a larger percentage of Aβ-LTMRs than centering the active contact above the ganglion.

When the active contact was centered directly above the ganglion (i.e. with a 0 mm electrode shift), anodic-first DRGS (Figure 5a) activated 12% of Aδ-LTMRs, while cathodic-first DRGS (Figure 5c) activated less than 1% of modeled Aδ-LTMRs. When the active and return contacts straddled the ganglion, anodic-first (Figure 5b) and cathodic-first (Figure 5d) DRGS activated 2% and 3% of modeled Aδ-LTMRs, respectively. However, shifting the electrode lead 1 mm dorsally abolished all Aδ-LTMRs. We observed minimal activation in Aδ-HTMRs. Anodic-first DRGS activated 3% of modeled Aδ-HTMRs only during anodic-first DRGS when the active contact was centered directly above the ganglion (Figure 5a). Shifting the electrode lead 1 mm dorsally abolished all Aδ-HTMR activation. We did not observe Aδ-HTMR activation during cathodic-first DRGS (Figure 5c,d), nor during anodic-first DRGS when the active and return contacts straddled the ganglion (Figure 5b). We always observed a larger percentage of Aβ-LTMR activation than Aδ-neuron activation.

We observed Aα-neuron and Aβ-LTMR activation for all electrode positions. When the active contact was centered directly above the ganglion, anodic-first DRGS activated 100% and 92% of modeled Aα- and Aβ-neurons, respectively (Figure 5a), while cathodic-first DRGS activated 99% and 46% of modeled Aα- and Aβ-neurons, respectively (Figure 5c). When the active and return contacts straddled the DRG, anodic- and cathodic-first DRGS both activated 88% of modeled Aβ-LTMRs and more than 98% of modeled Aα-neurons (Figure 5b,d). Increasing the distance between the active contact and the ganglion decreased the percentage of both Aα- and Aβ-neurons activated by clinical DRGS. When the electrode lead was shifted dorsally 1 mm or greater from the ganglion, cathodic-first DRGS applied with the active and return contacts straddling the ganglion produced the greatest Aβ-LTMR activation (Figure 5d). When the electrode lead was shifted dorsally 3 mm from the ganglion, we only observed Aβ-LTMR activation when cathodic-first DRGS was applied with the active and return contacts straddled the ganglion (Figure 5d). We observed Aα-neuron activation regardless of the distance from the electrode lead distance to the ganglion.

Effect of stimulus pulse width

Stimulus pulse width is a critical parameter when programming a patient's DRGS system, and has been shown to affect neural activation (24) and paresthesia distribution (60) during SCS. Interestingly, increasing SCS pulse width lowered the activation threshold of small-diameter myelinated dorsal column axons (24). However, the effect of stimulus pulse width on neural activation during DRGS has not been rigorously studied. Therefore, we calculated primary afferent activation thresholds for several pulse widths (i.e. 100, 200, 300, 500, and 1000 μs) both when the active contact was centered above the ganglion, and when the active and return contacts straddled the DRG. Figure 6 shows the percentage of modeled neurons with activation thresholds in clinical range (i.e. ≤ 2 mA) as the stimulus pulse width increased, both when the active contact was centered above the ganglion, and when the active and return contacts straddled the ganglion.

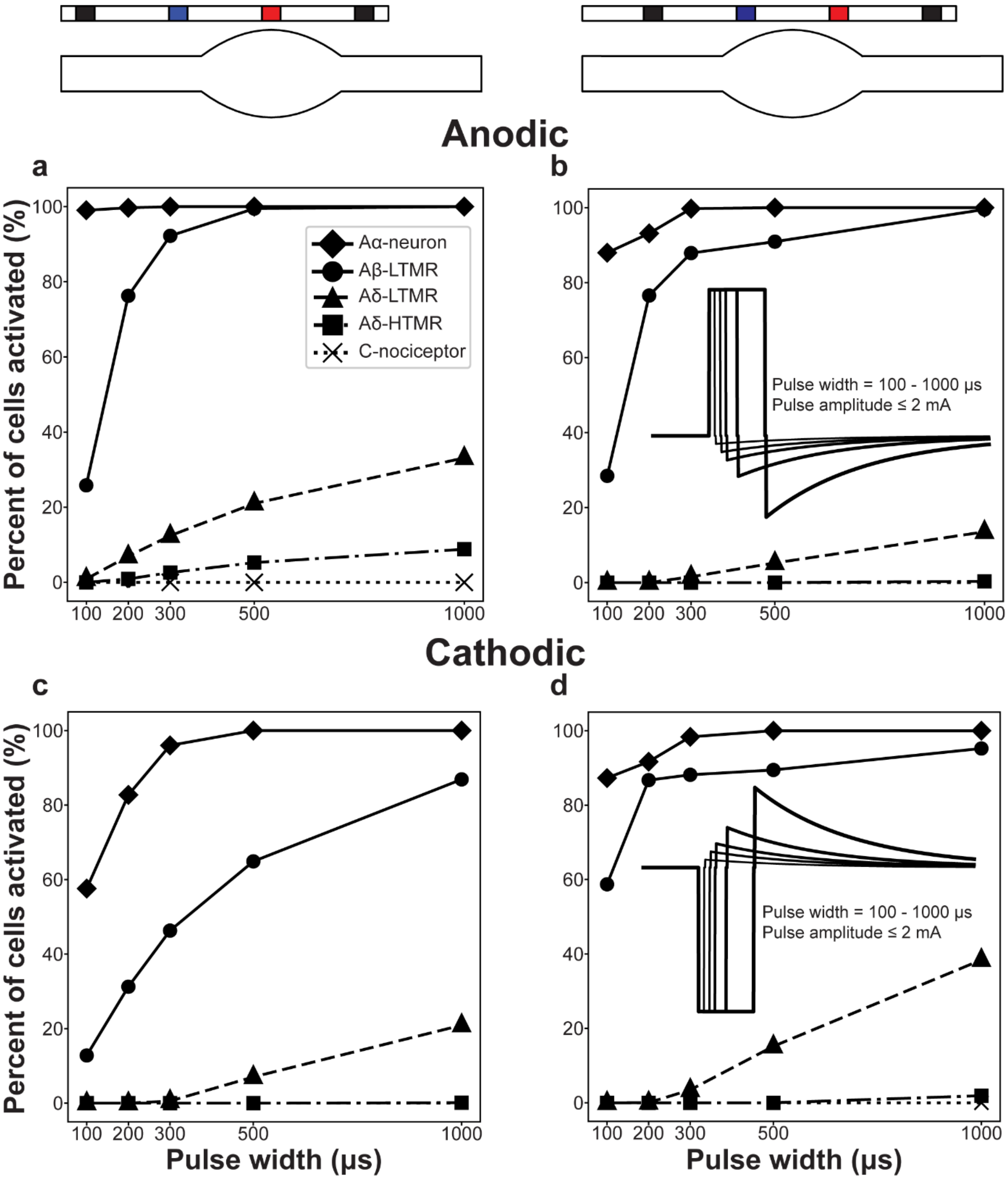

Figure 6: Effect of pulse width on neural activation during DRGS. Each plot shows the percentage of each neuron type that generated action potentials in response to DRGS with a pulse width between 100 μs and 1000 μs, and an amplitude 2 mA or less. We examined the effects of pulse width on neural activation for several electrode positions and stimulus polarities: the active (red) contact centered above the ganglion (a, c), the active and return (blue) contacts straddling the ganglion (b, d), anodic-first DRGS (a, b), and cathodic-first DRGS (c, d).

For amplitudes within the clinical range, we did not observe activation of nonmyelinated C-nociceptors for any pulse width. However, we did observe activation of small-diameter thinly-myelinated Aδ-neurons. When the active contact was centered above the ganglion, the minimum pulse widths for anodic-first DRGS (Figure 6a) to activate one or more Aδ-LTMRs or Aδ-HTMRs were 100 μs and 200 μs, respectively, while the minimum pulse widths for cathodic-first DRGS (Figure 6c) to activate one or more Aδ-LTMRs or Aδ-HTMRs were 300 μs and 1000 μs, respectively. When the active and return contacts straddled the ganglion, the minimum pulse widths for anodic-first DRGS to activate one or more Aδ-LTMRs or Aδ-HTMRs were 300 μs and 1000 μs, respectively (Figure 6b), while the minimum pulse widths for cathodic-first DRGS to activate one or more Aδ-LTMRs or Aδ-HTMRs were 200 μs and 1000 μs, respectively (Figure 6d). DRGS always recruited more Aδ-LTMRs than Aδ-HTMRs, regardless of pulse width or stimulus polarity.

We observed Aα- and Aβ-neuron activation by clinical DRGS for all pulse widths. Increasing the stimulus pulse width increased the percentage of Aα- and Aβ-neurons activated, regardless of stimulus pulse polarity or position of the active and return contact relative to the ganglion. For stimulus pulse widths below 300 μs, cathodic-first DRGS applied with the active and return contacts straddling the ganglion activated the largest percentage of Aβ-LTMRs (59-87%) (Figure 6d). For stimulus pulse widths greater than or equal to 300 μs, anodic-first DRGS applied with the active contact centered above the ganglion activated the largest percentage of Aβ-LTMRs (92-100%) (Figure 6a). Anodic-first DRGs applied with the active contact centered above the ganglion always activated the largest percentage of Aα-neurons (99-100%) (Figure 6a) For all pulse widths and stimulus polarities, there was always a larger percentage of Aα- and Aβ-neurons activated by clinical DRGS than any other neuron type.

Effect of stimulus pulse frequency

Stimulus pulse frequency is an important parameter during neurostimulator programming, and recent innovations in neurostimulation for pain have focused chiefly on this parameter (e.g. 10 kHz SCS (25)). DRGS is, on average, applied at 20 Hz, but can be applied as low as 4 Hz or as high as 80 Hz (26). Presently, we do not understand the physiological effect of varying stimulus pulse frequency, nor how those effects translate to clinical outcomes. Therefore, we applied anodic- and cathodic-first DRGS with a pulse amplitude of 1 mA, a pulse width of 300 μs, and examined the time-varying membrane potential of different neural compartments (e.g. soma, axons) in response to DRGS applied at different pulse frequencies.

Regardless of pulse frequency, we did not observe activation of nonmyelinated C-nociceptors for any stimulus pulse frequency, for DRGS applied within standard clinical parameter ranges. We observed minimal activation of both thinly myelinated Aδ-LTMRs and Aδ-HTMRs (a maximum of 12% and 3%, respectively). As the majority of our data suggests that DRGS predominantly activates large myelinated neurons, and Aβ-LTMRs are believed to play an important role in both DRGS-induced pain relief and physiologic pain inhibition in the spinal cord, (19, 61), we focused the rest of our analyses on Aβ-LTMRs.

Figure 7 shows the average response frequency of different Aβ-LTMR compartments (i.e. soma, stem axon, centrally-projecting axon, peripherally-projecting axon) to DRGS applied at different frequencies, for Aβ-LTMRs that responded to DRGS applied with a 1 mA stimulus pulse. For most stimulus polarities and positions of active and return contacts, all Aβ-LTMR compartments responded in a one-to-one fashion with the DRGS pulse (i.e. one action potential for each stimulus pulse). However, in response to anodic-first DRGS with the

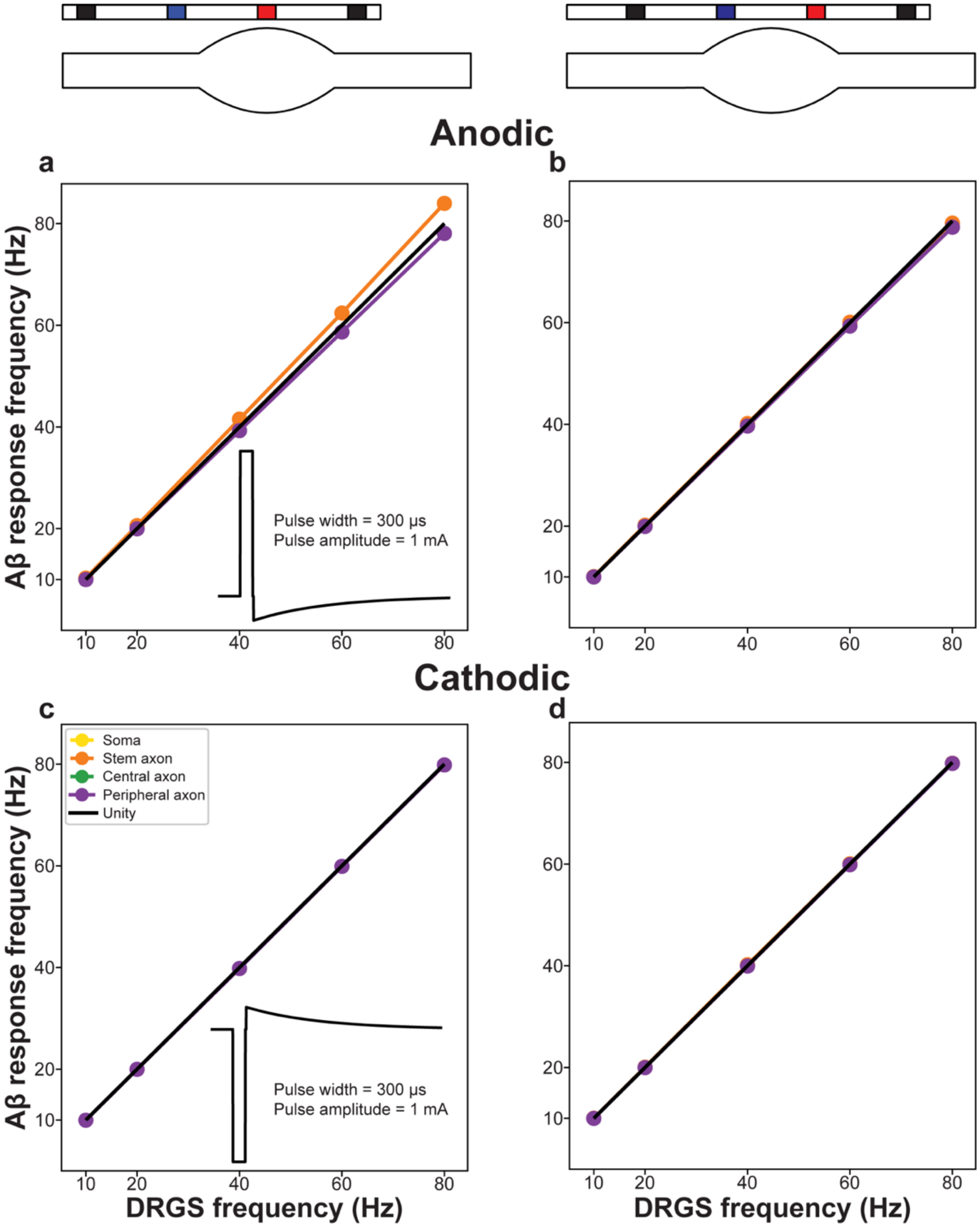

Figure 7: Effect of pulse frequency on different Aβ-LTMR compartment response frequencies during DRGS. Each plot shows the average response frequency (i.e. the frequency of action potential generation in response to DRGS) of Aβ-LTMR somata (blue), stem axons (orange), centrally-projecting axons (green), and peripherally projecting axons (red). The black lines indicate unity (i.e. the neural compartment is responding in a one-to-one fashion with the stimulus train). We examined the effects of pulse frequency for several electrode positions and stimulus polarities: the active (red) contact centered above the ganglion (a, c), the active and return contacts straddling the ganglion (b, d), anodic-first DRGS (a, b), and cathodic-first DRGS (c, d). Note: some data are not visible due to many compartments having the same response frequency.

active contact centered above the ganglion, the stem axon's response frequency was slightly larger than unity, while all other compartments' response frequencies were slightly below unity (Figure 7a). The increase in stem axon response frequency was caused by a rebound action potential propagating down the stem axon following a somatic action potential, which fails to propagate passed the T-junction. The decrease in the average response frequencies in other compartment was attributed to neurons with activation thresholds near 1 mA. For those neurons, some DRGS pulses elicited an action potential, while some pulses failed to induce an action potential.

Effect of bipole placement

Clinical DRGS utilizes a bipolar stimulation configuration in which the cathode is typically placed directly beneath the pedicle (26). However, the position of the DRG within the foramen varies across patients and spinal level (27, 62). X-ray fluoroscopy, the imaging modality used to visualize electrode position relative to bony structures during DRGS electrode implantation, is unable to resolve neural tissue, implying that clinicians are unable to precisely determine the position of the ganglia relative to the active contact. Therefore, the position of the stimulating contacts relative to the DRG is likely variable across patients, warranting investigation into how bipole placement relative to the ganglion affects neural activation during DRGS.

Figure 8 shows the percentage of modeled Aβ-LTMRs activated by various bipolar DRGS configurations. For bipolar configurations where the active and return contacts were adjacent to each other (Figure 8a), cathodic-first DRGS (light gray bars) typically activated more Aβ-LTMRs than anodic-first DRGS (dark gray bars), except when the active contact was centered above the ganglion. Cathodic-first DRGS applied with the return contact centered above the ganglion, and the active contact above the peripheral nerve root, activated the largest percentage of modeled Aβ-LTMRs (99%). Anodic-first DRGS applied with the active electrode above the spinal nerve root activated the smallest percentage of modeled Aβ-LTMRs (40%). In general, placing the cathode near the peripheral nerve root, or placing the anode near the ganglion, maximized Aβ-LTMR activation.

For bipolar configurations with one or more inactive contacts separating the active and return contacts (i.e. separated bipoles; Figure 8b), cathodic-first DRGS typically activated more Aβ-LTMRs than anodic-first DRGS. For separated bipole configurations, anodic-first DRGS only activated more Aβ-LTMRs than cathodic-first DRGS when the active contact was centered above the ganglion, similar to bipolar DRGS with adjacent active and return contacts. Three separated bipole configurations activated more than 98% of modeled Aβ-LTMRs, each of which applied cathodic-first DRGS with the active contact above the peripheral nerve root, and the return contact as either the first or second most proximal contact. Anodic-first DRGS applied with a distal active contact and proximal return contact (i.e. placing the active contact above the peripheral nerve root and the return contact above the spinal root) activated the smallest percentage of modeled Aβ-LTMRs (37%). Similar to adjacent bipole configurations, placing the cathode near the peripheral nerve root, or placing the anode near the ganglion, maximized Aβ-LTMR activation. However, except for the case when the active electrode was centered above the ganglion, cathodic-first DRGS using a separated bipole configuration always

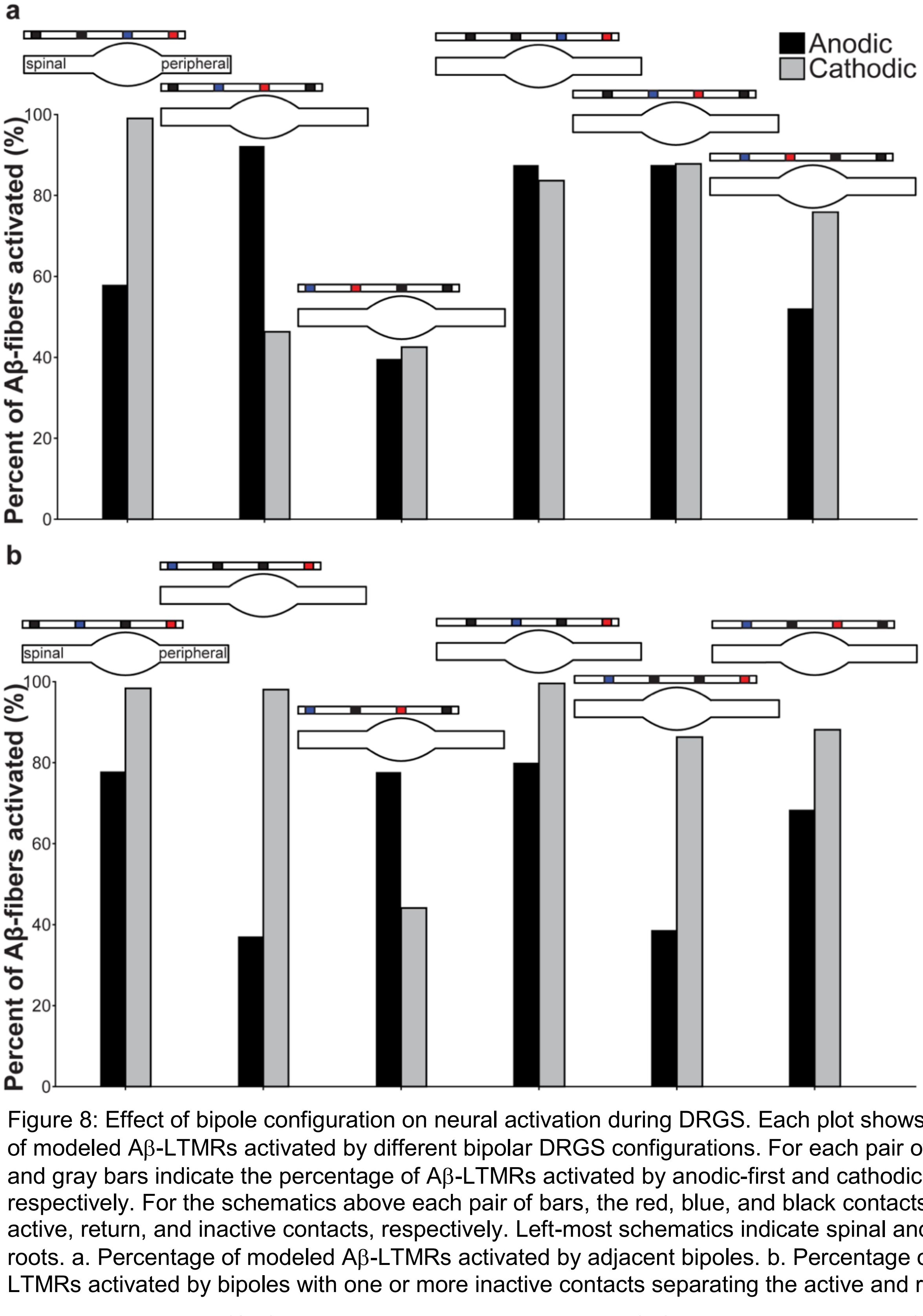

Figure 8: Effect of bipole configuration on neural activation during DRGS. Each plot shows the percentage of modeled Aβ-LTMRs activated by different bipolar DRGS configurations. For each pair of bars, the black and gray bars indicate the percentage of Aβ-LTMRs activated by anodic-first and cathodic-first DRGS, respectively. For the schematics above each pair of bars, the red, blue, and black contacts indicate the active, return, and inactive contacts, respectively. Left-most schematics indicate spinal and peripheral nerve roots. a. Percentage of modeled Aβ-LTMRs activated by adjacent bipoles. b. Percentage of modeled Aβ-LTMRs activated by bipoles with one or more inactive contacts separating the active and return contacts.

activated more than 80% of modeled Aβ-LTMRs, while only half of the adjacent bipole configurations activated more than 80% of modeled Aβ-LTMRs.

Effect of the guarded cathode stimulation configuration

Guarded cathode configurations are commonly used in clinical SCS (34), but to our knowledge have not been documented in DRGS studies. Therefore, we examined neural activation patterns resultant from DRGS applied with guarded cathode stimulation configurations. We again observed no activation of nonmyelinated C-nociceptors, and minimal activation of Aδ-LTMRs and Aδ-HTMRs (a maximum of 12% and 3%, respectively), and therefore we focused our analysis on Aβ-LTMRs.

Figure 9 shows the percentage of modeled Aβ-LTMRs activated by various guarded cathode DRGS configurations. Similar to conventional and longitudinal bipole configurations, anodic-first DRGS applied with a guarded active contact activated more Aβ-LTMRs than cathodic-first DRGS only when the active contact was centered above the ganglion. When the active contact was close to a nerve root, or when the active contact and one of the return contacts straddled the ganglion, cathodic-first DRGS activated more Aβ-LTMRs than anodic-first DRGS. For guarded active contact configurations, applying anodic-first DRGS with the active contact centered above the ganglion maximized Aβ-LTMR activation (89%). For cathodic-first DRGS applied with a guarded active contact configuration, placing the active contact near the peripheral nerve root maximized Aβ-LTMR activation (87%).

Discussion

DRGS is a safe and effective therapy for chronic pain that is refractory to conventional medical management. To ensure accurate delivery of electrical stimulation to the DRG, several clinically-controllable

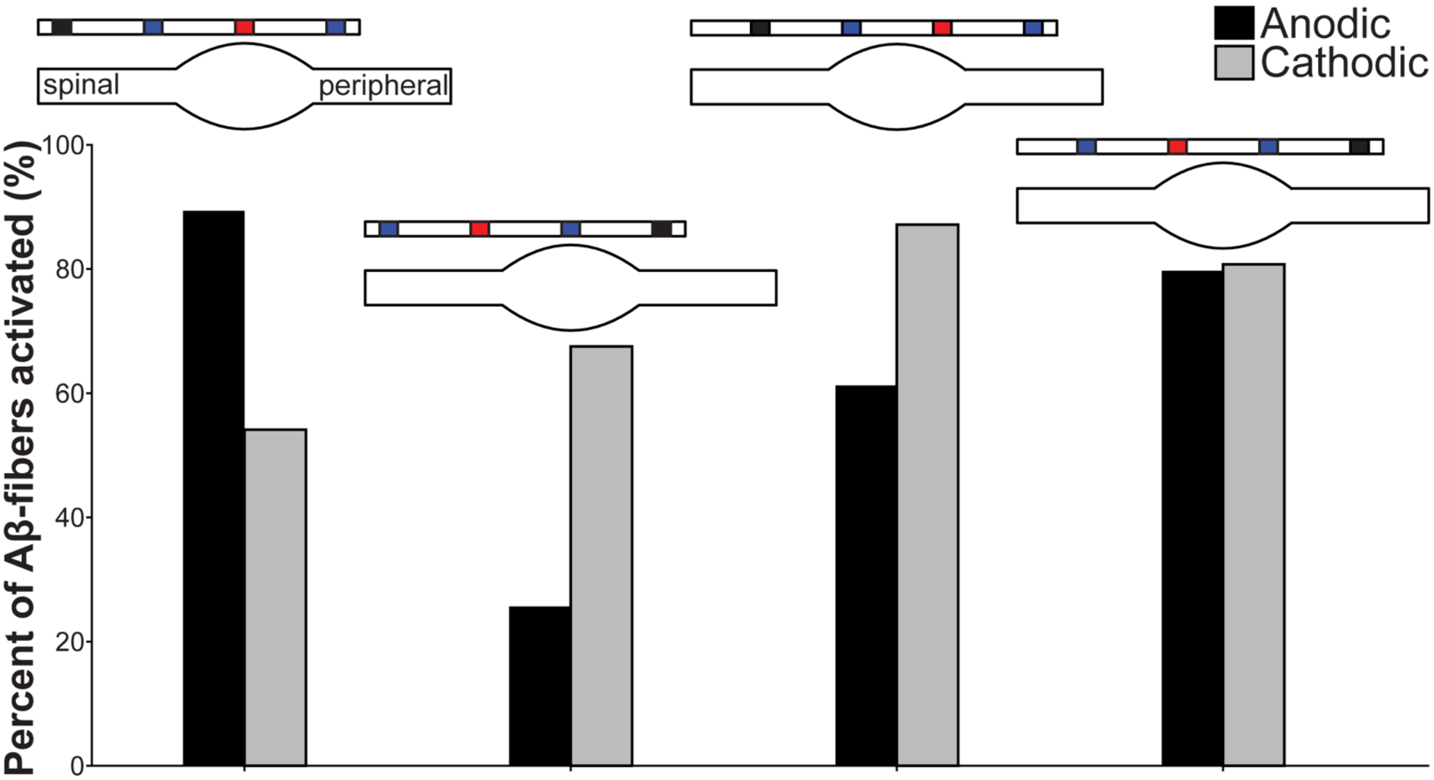

Figure 9: Effect of guarded active contact configurations on neural activation during DRGS. For each pair of bars, the black and gray bars indicate the percentage of Aβ-LTMRs activated by anodic-first and cathodic-first DRGS, respectively. For the schematics above each pair of bars, the red, blue, and black contacts indicate the active, return, and inactive contacts, respectively. Left-most schematic indicates spinal and peripheral nerve roots.

parameters, such as the position of the active and return contacts and the shape of the stimulus pulse, must be carefully tuned to maximize pain relief without producing uncomfortable sensations. It is presently unclear how varying each of these parameters affects which types of sensory neurons are directly activated by DRGS. Our data suggest that DRGS applied with stimulation amplitudes within a clinical range (i.e. ≤ 2 mA) predominantly activates large-diameter myelinated afferents (e.g. Aα- and Aβ-neurons). Furthermore, our results indicate that the position of the active and return contacts relative to the ganglion has the greatest effect on DRGS-induced Aβ-LTMR activation.

Implications for mechanisms of DRGS

Our data suggest that clinical DRGS directly activates myelinated neurons, regardless of electrode position, stimulation configuration, and stimulus pulse parameters (i.e. frequency, pulse width). This corroborates our previous study's findings that clinical DRGS is likely driving the activity of large-diameter myelinated Aβ-LTMRs, without directly activating small-diameter nonmyelinated C-nociceptors (19), and is supported by recent experimental findings that DRGS applied with non-penetrating electrode arrays activates neurons with conduction velocities in the Aδ- to Aβ-axon range (63). Furthermore, our data also suggest that clinical DRGS activates Aα-neurons, and may activate Aδ-neurons, though in a considerably smaller proportion than Aα- and Aβ-neurons. Based on these findings, DRGS may provide pain relief by driving pain-gating mechanisms in the dorsal horn, via postsynaptic activation of inhibitory interneurons which receive input from large myelinated afferents. This hypothesis suggests similarities between the mechanisms of DRGS and SCS. Previous animal studies of SCS demonstrated increased levels of γ-aminobutyric acid (GABA), an inhibitory neurotransmitter, in the spinal cord (64), and increased paw withdrawal thresholds in animals that responded to SCS (65) predominantly driven through the GABA_B receptor (66, 67). However, a recent study in rats concluded that DRGS does not cause GABA release in the dorsal horn (68), indicating DRGS may provide pain relief through other mechanisms.

Koetsier and colleagues suggested that instead of driving GABAergic inhibition in the dorsal horn, DRGS may provide pain relief by inducing GABAergic inhibition through GABA signaling within the DRG (68). Du and colleagues concluded that in rats, activating small-, medium-, or large-diameter DRG neurons can induce GABA release in the DRG, and that nearly all small-diameter DRG neurons (putative nociceptors) can respond to GABA (69). Furthermore, they demonstrated that VGAT, the primary transporter for inhibitory neurotransmitter reuptake, was commonly found in DRG neurons that co-expressed 200 kDa neurofilament, a marker of myelinated afferents in rats. Optogenetically stimulating VGAT expressing DRG neurons produced a marked reduction in nocifensive behavior, and GABA_A receptor antagonists increased nocifensive behavior even when no noxious stimuli were present, suggesting that a GABAergic pain-gating system exists at the level of the DRG. Taking these findings in context with our model predictions, it is possible that clinical DRGS provides pain relief by directly activating medium- and large-diameter myelinated afferents, causing local GABA release in the DRG to inhibit nociceptive afferents, thereby preventing pain signals from reaching the central nervous system.

However, GABA is not the only inhibitory neurotransmitter in the spinal dorsal horn. Many dorsal horn neurons which release GABA co-release glycine, with some inhibitory postsynaptic currents in superficial dorsal horn laminae mediated exclusively by glycine (70). Recent studies have identified a glycinergic feed-forward dorsal horn circuit that gates mechanical allodynia, mediated by paravalbumin (PV) expressing interneurons in lamina IIi and III of the dorsal horn, which silence lamina II PKCγ+ interneurons that form excitatory synapses on projection neurons in lamina I (71–73). These PV+ interneurons receive afferent input from both Aβ- and Aδ-axons (73), and gate mechanical pain via pre- and post-synaptic inhibition of primary afferents and lamina II excitatory interneurons, respectively (72, 73). Subsequent studies uncovered novel neural circuits involved in, and further somatosensory functions of, glycinergic inhibition. Foster and colleagues demonstrated that selective ablation of dorsal horn interneurons which express GlyT2, the glycine transporter expressed in the spinal cord and brainstem, facilitates mechanical, heat, and cold hyperalgesia, and can induce spontaneous pain behaviors (74). Cui and colleagues identified a separate subpopulation of deep laminae (III-V), predominantly glycinergic interneurons which receive mono- and polysynaptic input from both A- and C-axons, and form a feed-forward gate to silence pain transmission from PKCγ+ and somatostatin+ superficial dorsal horn neurons (75). The results of these studies emphasize the complexity of sensory processing in the dorsal horn, and taken together with the data presented in this work, suggest that DRGS may provide pain relief through a combination of glycinergic inhibition in the dorsal horn and GABAergic inhibition within the DRG itself. To fully elucidate the mechanisms of action of DRGS, we must uncover how innocuous and noxious stimuli are processed in dorsal horn and supraspinal structures in healthy and pathological states, and how the pattern of DRGS-induced afferent activity augments or abrogates neural activity throughout the neuraxis.

Importance of electrode lead placement

The location of the DRGS electrode lead relative to the DRG likely varies across patients, depending on the size of the patients' neuroforamina, the position of their DRG within the foramen (27, 62), and the implanting physician's placement of the electrode lead relative to the patient's DRG. The NACC suggests that straddling the second and third contacts across the medial and lateral borders of the pedicle is the optimal position of the lead in the foramen (26). This positioning likely resembles our models where the second and third contacts are straddling the ganglion, as lumbar DRG are typically located in the 'foraminal zone' (i.e. beneath the pedicle) (27). Martin and colleagues found that power consumption by the implanted pulse generator (IPG) was minimized by electrodes placed superodorsally in the foramen, a similar position to what the NACC suggests to be optimal (58). However, Martin and colleagues found that clinical outcomes were not dependent on the position of the electrode in the foramen. That study suggests that DRGS is able to activate analgesic mechanisms with the electrode placed anywhere in the foramen, at the cost of additional power consumption, though the optimal electrode positioning would result in straddling the ganglion with the active and return contacts.

Our modeling results, and our hypothesis that DRGS provides pain relief by driving the activity of large-diameter myelinated afferents, corroborate these notions. We demonstrated that DRGS consistently activates

Aα- and Aβ-neurons regardless of the positioning of active and return contacts relative to the ganglion, selection of stimulus parameters, and distance between the electrode lead body and the ganglion (Figure 5). Furthermore, we showed that straddling the active and return contacts across the ganglion maximizes Aβ-LTMR activation (Figure 5d). Straddling the DRG with the active and return contacts, and placing the electrode lead in close proximity to the ganglion, would therefore enable consistent DRGS-induced analgesia while minimizing IPG power consumption, thereby reducing the need for battery replacement surgeries.

Importance of stimulator programming

Programming a patient's DRG stimulator is a crucial, and often time-consuming process, as the stimulus parameter space is large and cannot be fully explored in a single programming session. This process is further complicated by the fact that we do not fully understand how varying each parameter, such as pulse width, pulse frequency, and the placement of cathodes and anodes, affects neural recruitment during DRGS. The median DRGS pulse width and pulse frequency reported by the ACCURATE trial were 300 μs and 20 Hz respectively, and the NACC highlights that pulse widths utilized by patients typically decrease over time, and that shorter pulse widths maximize the therapeutic window (26). Our results again corroborate the NACC recommendations; we demonstrated that regardless of pulse width, DRGS is predominantly activating Aβ-LTMRs, especially with shorter pulse widths (Figure 6). However, when using 500 μs or 1000 μs pulse widths, our models predicted increased activation of both Aδ-LTMRs and Aδ-HTMRs (Figure 6a,d). Activation of smaller diameter axons in response to longer pulse widths has also been reported in SCS studies, where increased pulse widths increased activation of small diameter myelinated axons in the medial dorsal columns (24, 36). Increased activation of Aδ-neurons, particularly Aδ-HTMRs, could explain why some patients report uncomfortable or painful sensations in response to DRGS of longer pulse widths. Therefore, shorter pulse widths (i.e. ≤ 300 μs) may maximize activation of target neurons (i.e. Aβ-LTMRs), while minimizing activation of nociceptive neurons, increasing the therapeutic window of DRGS.

From the ACCURATE clinical trial, the median DRGS pulse frequency was 20 Hz, and the maximum frequency across the DRGS patient cohort did not exceed 50 Hz at any time point (9). Our data demonstrate that in general, DRGS elicits one-to-one action potential generation in most Aβ-LTMRs (Figure 7), suggesting DRGS consistently sends propagating action potentials to the dorsal horn via Aβ-LTMRs. However, our data do not explain why DRGS patients typically utilize lower frequencies (around 20 Hz on average) compared to SCS patients (around 50 Hz on average (76)), especially considering the two therapies may operate through similar mechanisms (i.e. driving the activity of Aβ-LTMRs in the DRG vs. in the dorsal columns). Future experimental and clinical studies are necessary to understand the effect of DRGS pulse frequency both on the mechanisms of the therapy and on clinical outcomes.

As described above, the NACC suggests straddling the second and third contacts across the target pedicle and applying bipolar, cathodic-first DRGS. However, it is currently unknown how selecting contacts as anodes and cathodes affects neural activation during DRGS. We showed that regardless of which contacts were set to be active, DRGS activated a substantial portion (~40%) of modeled Aβ-LTMRs (Figure 8).

Generally, placing an anode near the body of the ganglion, or placing a cathode near a nerve root, particularly near the peripheral nerve root which contains larger-diameter axons, maximized Aβ-LTMR activation. This agrees with our previous findings (19), and follows conventional neurostimulation theory that anodic stimulation results in lower activation thresholds when the electrode is near a cell body, and cathodic stimulation results in lower activation thresholds when the electrode is near an axon of passage (22).

Guarded cathode configurations, placing an anode on either side of a cathode, are commonly used in traditional SCS. Because traditional SCS putatively targets the dorsal columns – axons of passage running parallel to the implanted electrode – guarded cathodes are thought to maximize the therapeutic window of SCS by maximizing the activating function along dorsal column axons (77). We explored if DRGS applied with a guarded active contact configuration would provide greater Aβ-LTMR activation than other stimulus configurations. However, we did not find any added benefit of the guarded cathode configuration compared to bipolar configurations, regardless of stimulus polarity (Figures 8, 9). As DRG neurons are not axons of passage, but instead have pseudounipolar morphologies (14), the guarded cathode configuration is unlikely to maximize neural activation during DRGS. Our data again add support to the NACC recommendation that ‘complex programming arrays are not necessary, as simple bipolar arrays can achieve optimal activation of the DRG,’ (26).

Limitations

Although we built our models using previously-published clinical and experimental data, there are several limitations to our approach. The FEM of a human L5 DRG used in this study represented several anatomical compartments (e.g. foraminal bone, intraforaminal tissue) as largely concentric cylinders. Although the method of representing anatomical compartments as simplified concentric shapes has been commonly used to study other clinical neurostimulation therapies (25, 78), recent work demonstrated that the complex anatomy of bony structures in the spine can affect model predictions of SCS-induced neural activation (23). Future studies could employ a patient-specific modeling approach, similar to previous studies of SCS (79), which could elucidate how the complex anatomy of the spinal column affects DRGS model predictions.

Human lumbar DRG somata are typically located around the dorsal edge of the ganglion (54). To study how DRGS would affect a specific cell type at any location in the DRG, we homogeneously distributed each cell type throughout the DRG, with their cell bodies placed around the dorsal edge of the ganglion. However, the actual distribution of functional subpopulations of DRG neurons (e.g. Aα-neurons) is likely not homogeneous. Our data suggest DRGS causes widespread activation of large diameter Aα-neurons, which carry proprioceptive and stretch-receptor information from the muscles. However, a recent study in mice lumbar DRG showed that only 0.6% of DRG neurons were PV+, a marker of proprioceptive primary afferents (80), and our recent histological data suggests that only 3.6% of axons in human lumbar DRG have diameters greater than or equal to 12 μm, an approximate lower limit of Aα-axon diameters (54, 81, 82). Furthermore, human lower leg muscles contain on the order of hundreds of muscle spindles (83), while there are tens of thousands of neurons in human DRG (54). These data suggest that Aα-neurons may sparsely populate the

DRG, and therefore our model may be overestimating the amount of Aα-neuron activation during clinical DRGS. However, prolonged activation of muscle afferents could be another source of DRGS-induced discomfort, in addition to the activation of Aδ-neurons with longer stimulus pulse widths described above. Future studies should examine the functional organization of cells within human DRG and the corresponding implications for DRGS.

We modeled several classes of neurons important to the transmission of painful and non-painful stimuli: Aα-, Aβ-, Aδ-, and C-neurons. However, we ignored the potential effects of DRGS on non-neuronal DRG cells, such as satellite glial cells (SGCs), the glial cell type found in DRG. Glial cells in the central nervous system are known to play an important role in regulating both normal nociceptive pain processing and pathological chronic pain states (84, 85). Furthermore, recent work has highlighted the contributions of SGCs to chronic pain, including visceral pain (86). To date, there are few studies examining the influence of clinical neurostimulation therapies on glial activity, though the effect of SCS-induced electric fields on glial cell function is a growing area of study (87–89). Glial cells express voltage-gated ion channels, the molecular targets by which neurostimulation therapies influence neural activity (90). Though SGCs do not contain voltage-gated sodium channels, the channel chiefly responsible for the generation of propagating action potentials, SGCs do express voltage-gated potassium channels (91). The extent to which DRGS affects voltage-gated channels in SGCs is unclear, though it is possible that DRGS could indirectly induce a myriad of potassium-mediated intracellular signaling cascades within SGCs. This notion is supported by recent studies highlighting the importance of glial cells in the development and maintenance of chronic pain at multiple levels of the nervous system, such as Schwann cells in the periphery (92), SGCs themselves in the DRG (93), and microglia in the spinal dorsal horn (94).

Finally, we examined the direct neural response to DRGS, i.e. which neurons are directly activated by one DRGS pulse or a short train of DRGS pulses. Clinically, DRGS is applied tonically, ideally over the period of years. In our multi-compartment neuron models, we included models of voltage-gated sodium and potassium channels, but ignored the contributions of other types of ion channels, such as calcium channels. We believe that this simplification is justified for examining the direct neural response to DRGS, as voltage gated sodium and potassium channels are predominantly responsible for the generation of action potentials (95). However, due to this simplification, we were unable to study the long-term effects of tonic DRGS, as these channels activate and inactivate on time scales ranging from a few to tens of milliseconds. Furthermore, computational demands are prohibitive in simulating more than a second of neural activity. To complete the picture of the effect of DRGS on primary afferents, future experimental studies should study the effect of long-term DRGS on physiological processes mediated by ion channels that operate on long timescales, and on how tonic DRGS may modulate cause up- or down-regulation of different genes (96).

Conclusion

DRGS is a valuable clinical tool for managing intractable focal pain. Currently, we do not understand the physiological mechanisms of action of DRGS, nor how the clinical implementation of DRGS (e.g. lead placement, stimulator programming) affects the utilization of these mechanisms. In this work, we studied how clinically-controllable parameters affect neural activation during DRGS. Firstly, our data support the hypothesis that DRGS provides pain relief by directly activating Aβ-LTMRs, leading to postsynaptic activation of pain-gating mechanisms in the dorsal horn and possibly pain-gating mechanisms within the DRG itself. Based on this hypothesis, our data corroborate several NACC recommendations: 1) straddling the active and return contacts across the pedicle (and presumably, the ganglion) may be the optimal electrode positioning in the foramen, 2) shorter pulse widths are preferred, based on maximizing activation of innocuous neurons while minimizing activation of potentially nociceptive neurons, and 3) conventional bipolar stimulation is sufficient to achieve analgesia, without the need for more complex programming configurations. Although the data presented here are pivotal to understanding the direct neural response to DRGS, future experimental and clinical studies are necessary to understand the downstream mechanisms of DRGS and how such effects influence long-term success with the therapy.

Acknowledgements

The authors would like to thank Dr. Marco Capogrosso (University of Pittsburgh, Pittsburgh, PA, USA) for his helpful feedback on this work. This work was supported in part through computational resources provided by Advanced Research Computing at the University of Michigan, Ann Arbor and by the National Science Foundation (NSF CAREER award 1653080).

References

1. Nahin RL. Estimates of pain prevalence and severity in adults: United States, 2012. *J Pain* 2015;16(8):769-780. doi:10.1016/j.jpain.2015.05.002
2. Paulozzi LJ, Jones CM, Mack KA, Rudd RA. Vital signs: Overdoses of prescription opioid pain relievers - United States, 1999-2008. *MMWR Morb Mortal Wkly Rep* 2011;60(43):1487-1492.
3. Rudd RA, Aleshire N, Zibbell JE, Gladden RM. Increases in drug and opioid overdose deaths - United States, 2000-2014. *MMWR Morb Mortal Wkly Rep* 2016;64:1378-1382.
4. Scholl L, Seth P, Kariisa M, Wilson N, Baldwin G. Drug and opioid-involved overdose deaths - United States, 2013-2017. *MMWR Morb Mortal Wkly Rep* 2019;67:1419-1427. doi:10.15585/mmwr.mm675152e1
5. Kumar K, Taylor RS, Jacques L, Eldabe S, Meglio M, Molet J, et al. The effects of spinal cord stimulation in neuropathic pain are sustained: A 24-month follow-up of the prospective randomized controlled multicenter trial of the effectiveness of spinal cord stimulation. *Neurosurgery* 2008;63(4):762-768. doi:10.1227/01.NEU.0000325731.46702.D9
6. Lempka SF, Patil PG. Innovations in spinal cord stimulation for pain. *Curr Opin Biomed Eng* 2018;8:51-60. doi:10.1016/j.cobme.2018.10.005
7. Kumar K, Rizvi S, Bnurs SB. Spinal cord stimulation is effective in management of complex regional pain syndrome I: Fact or fiction. *Neurosurgery* 2011;69(3):566-578. doi:10.1227/NEU.0b013e3182181e60
8. Deer TR, Pope JE. Dorsal root ganglion stimulation approval by the Food and Drug Administration:

Advice on evolving the process. *Expert Rev Neurother* 2016;16(10):1123-1125. doi:10.1080/14737175.2016.1206817

9. Deer TR, Levy RM, Kramer J, Poree L, Amirdelfan K, Grigsby E, et al. Dorsal root ganglion stimulation yielded higher treatment success rate for CRPS and causalgia at 3 and 12 months. *Pain* 2017;158(4):669-681. doi:10.1097/j.pain.0000000000000814
10. Eldabe S, Burger K, Moser H, Klase D, Schu S, Wahlstedt A, et al. Dorsal root ganglion (DRG) stimulation in the treatment of phantom limb pain (PLP). *Neuromodulation* 2015;18:610-617. doi:10.1111/ner.12338
11. Eldabe S, Espinet A, Wahlstedt A, Kang P, Liem L, Patel NK, et al. Retrospective case series on the treatment of painful diabetic peripheral neuropathy with dorsal root ganglion stimulation. *Neuromodulation* 2018;21:787-792. doi:10.1111/ner.12767
12. Morgalla MH, Bolat A, Fortunato M, Lepski G, Chander BS. Dorsal root ganglion stimulation used for the treatment of chronic neuropathic pain in the groin: A single-center study with long-term prospective results in 34 cases. *Neuromodulation* 2017;20:753-760. doi:10.1111/ner.12713
13. Haberberger RV, Barry C, Dominguez N, Matusica D. Human dorsal root ganglia. *Front Cell Neurosci* 2019;13:1-17. doi:10.3389/fncel.2019.00271
14. Devor M. Unexplained peculiarities of the dorsal root ganglion. *Pain* 1999;82(Supplement 6):S27-S35.
15. Morgalla MH, Fortunato M, Lepski G, Chander BS. Dorsal root ganglion stimulation (DRGS) for the treatment of chronic neuropathic pain: A single-center study with long-term prospective results in 62 Cases. *Pain Physician* 2018;21(4):E377-E388.
16. Sears NC, Machado AG, Nagel SJ, Deogaonkar M, Stanton-Hicks M, Rezai AR, et al. Long-term outcomes of spinal cord stimulation with paddle leads in the treatment of complex regional pain syndrome and failed back surgery syndrome. *Neuromodulation* 2011;14:312-318. doi:10.1111/j.1525-1403.2011.00372.x
17. Nissen M, Ikäheimo T-M, Huttunen J, Leinonen V, von und zu Fraunberg M. Long-term outcome of spinal cord stimulation in failed back surgery syndrome: 20 years of experience with 224 consecutive patients. *Neurosurgery* 2019;84(5):1011-1018. doi:10.1093/neuros/nyy194
18. Kent AR, Min X, Hogan QH, Kramer JM. Mechanisms of dorsal root ganglion stimulation in pain suppression: A computational modeling analysis. *Neuromodulation* 2018;21:234-246. doi:10.1111/ner.12754
19. Graham RD, Bruns TM, Duan B, Lempka SF. Dorsal root ganglion stimulation for chronic pain modulates Aβ-fiber activity but not C-fiber activity: A computational modeling study. *Clin Neurophysiol* 2019;130(6):941-951. doi:10.1016/j.clinph.2019.02.016
20. Boyd IA, Kalu KU. Scaling factor relating conduction velocity and diameter for myelinated afferent nerve fibres in the cat hind limb. *J Physiol* 1979;289:277-297.
21. Abraira VE, Ginty DD. The sensory neurons of touch. *Neuron* 2013;79(4):618-639. doi:10.1016/j.neuron.2013.07.051
22. McIntyre CC, Grill WM. Excitation of central nervous system neurons by nonuniform electric fields.

Biophys J 1999;76(2):878-888. doi:10.1016/S0006-3495(99)77251-6

23. Anaya CJ, Zander HJ, Graham RD, Sankarasubramanian V, Lempka SF. Evoked potentials recorded from the spinal cord during neurostimulation for pain: A computational modeling study. *Neuromodulation* 2020;23(1):64-73. doi:10.1111/ner.12965
24. Lee D, Hershey B, Bradley K, Yearwood T. Predicted effects of pulse width programming in spinal cord stimulation: A mathematical modeling study. *Med Biol Eng Comput* 2011;49:765-774. doi:10.1007/s11517-011-0780-9
25. Lempka SF, McIntyre CC, Kilgore KL, Machado AG. Computational analysis of kilohertz frequency spinal cord stimulation for chronic pain management. *Anesthesiology* 2015;122(6):1362-1376. doi:10.1097/ALN.0000000000000649
26. Deer TR, Pope JE, Lamer TJ, Grider JS, Provenzano D, Lubenow TR, et al. The neuromodulation appropriateness consensus committee on best practices for dorsal root ganglion stimulation. *Neuromodulation* 2019;22(1):1-35. doi:10.1111/ner.12845
27. Hasegawa T, Mikawa Y, Watanabe R, An HS. Morphometric analysis of the lumbrosacral nerve roots and dorsal root ganglia by magnetic resonance imaging. *Spine* 1996;21(9):1005-1009.
28. Hogan Q. Size of human lower thoracic and lumbosacral nerve roots. *Anesthesiology* 1996;85:37-42. doi:10.1167/8.5.1.
29. Reina MA, Villanueva MC, López A, De Andrés JA. Grasa dentro de los manguitos durales de las raices nerviosas de la columna lumbar humana. *Rev Esp Anestesiol Reanim* 2007;54:297-301.
30. Amirdelfan K, Kramer J, Cusack WF, Burton AW. Advanced neuromodulation techniques: Dorsal root ganglion stimulation. In: *Advanced Procedures for Pain Management: A Step-by-Step Atlas*. Springer International Publishing; 2018:265-279.
31. Geddes LA, Baker LE. The specific resistance of biological material - a compendium of data for the biomedical engineer and physiologist. *Med Biol Eng* 1967;5(3):271-293. doi:10.1007/BF02474537
32. Gabriel S, Lau RW, Gabriel C. The dielectric properties of biological tissues: III. Parametric models for the dielectric spectrum of tissues. *Phys Med Biol* 1996;41(11):2271-2293. doi:10.1088/0031-9155/41/11/003
33. Grill WM, Mortimer JT. Electrical properties of implant encapsulation tissue. *Ann Biomed Eng* 1994;22:23-33. doi:10.1007/BF02368219
34. Holsheimer J, Wesselink WA. Optimum electrode geometry for spinal cord stimulation: The narrow bipole and tripole. *Med Biol Eng Comput* 1997;35:493-497. doi:10.1007/BF02525529
35. Holsheimer J, Wesselink WA. Effect of anode-cathode configuration on paresthesia coverage in spinal cord stimulation. *Neurosurgery* 1997;41(3):654-660. doi:10.1097/00006123-199709000-00030
36. Holsheimer J, Buitenweg JR, Das J, De Sutter P, Manola L, Nuttin B. The effect of pulse width and contact configuration on paresthesia coverage in spinal cord stimulation. *Neurosurgery* 2011;68(5):1452-1461. doi:10.1227/NEU.0b013e31820b4f47
37. Hines ML, Carnevale NT. The NEURON simulation environment. *Neural Comput* 1997;9:1179-1209. doi:10.1162/neco.1997.9.6.1179

38. Djouhri L, Bleazard L, Lawson SN. Association of somatic action potential shape with sensory receptive properties in guinea-pig dorsal root ganglion neurones. *J Physiol* 1998;513(3):857-872. doi:10.1111/j.1469-7793.1998.857ba.x

39. Bennett DL, Clark AJ, Huang J, Waxman SG, Dib-Hajj SD. The role of voltage-gated sodium channels in pain signaling. *Physiol Rev* 2019;99:1079-1151. doi:10.1152/physrev.00052.2017

40. Black JA, Dib-Hajj S, McNabola K, Jeste S, Rizzo MA, Kocsis JD, et al. Spinal sensory neurons express multiple sodium channel α-subunit mRNAs. *Mol Brain Res* 1996;43:117-131. doi:10.1016/S0169-328X(96)00163-5

41. Djouhri L, Newton R, Levinson SR, Berry CM, Carruthers B, Lawson SN. Sensory and electrophysiological properties of guinea-pig sensory neurones expressing Nav 1.7 (PN1) Na+ channel α subunit protein. *J Physiol* 2003;546(2):565-576. doi:10.1113/jphysiol.2002.026559

42. Djouhri L, Fang X, Okuse K, Wood JN, Berry CM, Lawson SN. The TTX-resistant sodium channel Nav1.8 (SNS/PN3): Expression and correlation with membrane properties in rat nociceptive primary afferent neurons. *J Physiol* 2003;550(3):739-752. doi:10.1113/jphysiol.2003.042127

43. Yoshida S, Matsuda Y. Studies on sensory neurons of the mouse with intracellular-recording and horseradish peroxidase-injection techniques. *J Neurophysiol* 1979;42(4):1134-1145. doi:10.1152/jn.1979.42.4.1134

44. McIntyre CC, Richardson AG, Grill WM. Modeling the excitability of mammalian nerve fibers: Influence of afterpotentials on the recovery cycle. *J Neurophysiol* 2002;87:995-1006. doi:10.1152/jn.00353.2001

45. McIntyre CC, Grill WM, Sherman DL, Thakor N V. Cellular effects of deep brain stimulation: Model-based analysis of activation and inhibition. *J Neurophysiol* 2004;91(4):1457-1469. doi:10.1152/jn.00989.2003

46. Ha H. Axonal bifurcation in the dorsal root ganglion of the cat: A light and electron microscopic study. *J Comp Neurol* 1970;140:227-240. doi:10.1002/cne.901400206

47. Capogrosso M, Gandar J, Greiner N, Moraud EM, Wenger N, Shkorbatova P, et al. Advantages of soft subdural implants for the delivery of electrochemical neuromodulation therapies to the spinal cord. *J Neural Eng* 2018;15:1-15. doi:10.1088/1741-2552/aaa87a

48. Gaines JL, Finn KE, Slopsema JP, Heyboer LA, Polasek KH. A model of motor and sensory axon activation in the median nerve using surface electrical stimulation. *J Comput Neurosci* 2018;45(1):29-43. doi:10.1007/s10827-018-0689-5

49. Sheets PL, Jackson JO, Waxman SG, Dib-hajj SD, Cummins TR. A Nav 1.7 channel mutation associated with hereditary erythromelalgia contributes to neuronal hyperexcitability and displays reduced lidocaine sensitivity. *J Physiol* 2007;581(3):1019-1031. doi:10.1113/jphysiol.2006.127027

50. Mainen ZF, Sejnowski TJ. Dendritic structure modulates firing pattern in model neocortical neurons. *Nature* 1996;382:363-366.

51. Stebbing MJ, Eschenfelder S, Acosta MC, Mclachlan EM, Universita C, Kiel Å, et al. Changes in the action potential in sensory neurones after peripheral axotomy in vivo. *Neuroreport* 1999;10:201-206.

52. Waddell PJ, Lawson SN. Electrophysiological properties of subpopulations of rat dorsal root ganglion

neurons in vitro. *Neuroscience* 1990;36(3):811-822. doi:10.1016/0306-4522(90)90024-X

53. Ostrowski AK, Sperry ZJ, Kulik G, Bruns TM. Quantitative models of feline lumbosacral dorsal root ganglia neuronal cell density. *J Neurosci Methods* 2017;290:116-124. doi:10.1016/j.jneumeth.2017.07.018
54. Sperry ZJ, Graham RD, Peck-Dimit N, Lempka SF, Bruns TM. Spatial models of cell distribution in human lumbar dorsal root ganglia. *J Comp Neurol* 2020:1-16. doi:10.1002/cne.24848
55. Hines ML, Davison AP, Muller E. NEURON and Python. *Front Neuroinform* 2009;3:1-12. doi:10.3389/neuro.11.001.2009
56. Moffitt MA, McIntyre CC. Model-based analysis of cortical recording with silicon microelectrodes. *Clin Neurophysiol* 2005;116(9):2240-2250. doi:10.1016/j.clinph.2005.05.018
57. Lempka SF, Howell B, Gunalan K, Machado AG, McIntyre CC. Characterization of the stimulus waveforms generated by implantable pulse generators for deep brain stimulation. *Clin Neurophysiol* 2018;129(4):731-742. doi:10.1016/j.clinph.2018.01.015
58. Martin S, Hadjipavlou G, Garcia Ortega R, Moir L, Edwards T, Bojanic S, et al. The importance of the location of dorsal root ganglion stimulator electrodes within the nerve root exit foramen. *Neuromodulation* 2019;(in press). doi:10.1111/ner.12959
59. Falowski SM, Conti KR, Mogilner AY. Analysis of S1 DRG programming to determine location of the DRG and ideal anatomic positioning of the electrode. *Neuromodulation* 2019;(in press). doi:10.1111/ner.13039
60. Yearwood TL, Hershey B, Bradley K, Lee D. Pulse width programming in spinal cord stimulation: a clinical study. *Pain Physician* 2010;13:321-335.
61. Duan B, Cheng L, Ma Q. Spinal circuits transmitting mechanical pain and itch. *Neurosci Bull* 2018;34(1):186-193. doi:10.1007/s12264-017-0136-z
62. Silverstein MP, Romrell LJ, Benzel EC, Thompson N, Griffith S, Lieberman IH. Lumbar dorsal root ganglia location: An anatomic and MRI assessment. *Int J Spine Surg* 2015;9. doi:10.14444/2003
63. Nanivadekar A, Ayers CA, Gaunt RA, Weber D, Fisher LE. Selectivity of afferent microstimulation at the DRG using epineural and penetrating electrode arrays. *J Neural Eng* 2019. doi:10.1088/1741-2552/ab4a24
64. Linderoth B, Stiller C-O, Gunasekera L, O'Connor WT, Ungerstedt U, Brodin E. Gamma-aminobutyric acid is released in the dorsal horn by electrical spinal cord stimulation: An in vivo microdialysis study in the rat. *Neurosurgery* 1994;34:484-489. doi:10.1017/CBO9781107415324.004
65. Janssen SP, Gerard S, Raijmakers ME, Truin M, Van Kleef M, Joosten EA. Decreased intracellular GABA levels contribute to spinal cord stimulation-induced analgesia in rats suffering from painful peripheral neuropathy: The role of KCC2 and GABAA receptor-mediated inhibition. *Neurochem Int* 2012;60:21-30. doi:10.1016/j.neuint.2011.11.006
66. Cui J-G, Linderoth B, Meyerson BA. Effects of spinal cord stimulation on touch-evoked allodynia involve GABAergic mechanisms. An experimental study in the mononeuropathic rat. *Pain* 1996;66(2-3):287-295. doi:10.1016/0304-3959(96)03069-2

67. Cui J-G, O'Connor WT, Ungerstedt U, Linderoth B, Meyerson BA. Spinal cord stimulation attenuates dorsal horn release of excitatory amino acids in mononeuropathy via a GABAergic mechanism. *Pain* 1997;73:87-95.

68. Koetsier E, Franken G, Debets J, Heijmans L, Kuijk SMJ, Linderoth B, et al. Mechanism of dorsal root ganglion stimulation for pain relief in painful diabetic polyneuropathy is not dependent on GABA release in the dorsal horn of the spinal cord. *CNS Neurosci Ther* 2019;00:1-8. doi:10.1111/cns.13192

69. Du X, Hao H, Yang Y, Huang S, Wang C, Gigout S, et al. Local GABAergic signaling within sensory ganglia controls peripheral nociceptive transmission. *J Clin Invest* 2017;127(5):1741-1756. doi:10.1172/JCI86812

70. Todd AJ. Identifying functional populations among the interneurons in laminae I-III of the spinal dorsal horn. *Mol Pain* 2017;13:1-19. doi:10.1177/1744806917693003

71. Lu Y, Dong H, Gao Y, Gong Y, Ren Y, Gu N, et al. A feed-forward spinal cord glycinergic neural circuit gates mechanical allodynia. *J Clin Invest* 2013;123(9):4050-4062.

72. Petitjean H, Pawlowski SA, Fraine SL, Sharif B, Hamad D, Fatima T, et al. Dorsal horn parvalbumin neurons are gate-keepers of touch-evoked pain after nerve injury. *Cell Rep* 2015;13(6):1246-1257. doi:10.1016/j.celrep.2015.09.080

73. Boyle KA, Gradwell MA, Yasaka T, Dickie AC, Polgár E, Ganley RP, et al. Defining a spinal microcircuit that gates myelinated afferent input: Implications for tactile allodynia. *Cell Rep* 2019;28(2):526-540.e6. doi:10.1016/j.celrep.2019.06.040

74. Foster E, Wildner H, Tudeau L, Haueter S, Ralvenius WT, Jegen M, et al. Targeted ablation, silencing, and activation establish glycinergic dorsal horn neurons as key components of a spinal gate for pain and itch. *Neuron* 2015;85(6):1289-1304. doi:10.1016/j.neuron.2015.02.028

75. Cui L, Miao X, Liang L, Abdus-Saboor I, Olson W, Fleming MS, et al. Identification of early RET+ deep dorsal spinal cord interneurons in gating pain. *Neuron* 2016;91(5):1137-1153. doi:10.1016/j.neuron.2016.07.038

76. Miller JP, Eldabe S, Buchser E, Johanek LM, Guan Y, Linderoth B. Parameters of Spinal Cord Stimulation and Their Role in Electrical Charge Delivery: A Review. *Neuromodulation* 2016;19(4):373-384. doi:10.1111/ner.12438

77. Moffitt MA, Lee DC, Bradley K. Spinal cord stimulation: Engineering approaches to clinical and physiological challenges. In: *Implantable Neural Prostheses 1*. ; 2009:155-194. doi:10.1007/978-0-387-77261-5

78. Datta A, Elwassif M, Battaglia F, Bikson M. Transcranial current stimulation focality using disc and ring electrode configurations: FEM analysis. *J Neural Eng* 2008;5(2):163-174. doi:10.1088/1741-2560/5/2/007

79. Lempka SF, Zander HJ, Anaya CJ, Wyant A, Ozinga JG, Machado AG. Patient-specific analysis of neural activation during spinal cord stimulation for pain. *Neuromodulation* 2019;2019. doi:10.1111/ner.13037

80. Giacobassi MJ, Leavitt LS, Raghuraman S, Alluri R, Chase K, Finol-Urdaneta RK, et al. An integrative

approach to the facile functional classification of dorsal root ganglion neuronal subclasses. *Proc Natl Acad Sci* 2020;117(10):1-8. doi:10.1073/pnas.1911382117

81. Peck-Dimit N, Sperry ZJ, Graham RD, Lempka SF, Bruns TM. Human DRG 3D cross section analysis. Open Science Framework. doi:10.17605/OSF.IO/TQRFZ
82. Hunt CC. Relation of function to diameter in afferent fibers of muscle nerves. *J Gen Physiol* 1954;38(1):117-131. doi:65.1678.208-a
83. Banks RW. An allometric analysis of the number of muscle spindles in mammalian skeletal muscles. *J Anat* 2006;208(6):753-768. doi:10.1111/j.1469-7580.2006.00558.x
84. Ji RR, Berta T, Nedergaard M. Glia and pain: Is chronic pain a gliopathy? *Pain* 2013;154(SUPPL. 1):S10-S28. doi:10.1016/j.pain.2013.06.022
85. Ji R-R, Donnelly CR, Nedergaard M. Astrocytes in chronic pain and itch. *Nat Rev Neurosci* 2019. doi:10.1038/s41583-019-0218-1
86. Hanani M. Role of satellite glial cells in gastrointestinal pain. *Front Cell Neurosci* 2015;9:1-10. doi:10.3389/fncel.2015.00412
87. Vallejo R, Bradley K, Kapural L. Spinal Cord Stimulation in Chronic Pain. *Spine* 2017;42(14):S53-S60. doi:10.1097/BRS.0000000000002179
88. Vallejo R, Gupta A, Kelley CA, Vallejo A, Rink J, Williams JM, et al. Effects of Phase Polarity and Charge Balance Spinal Cord Stimulation on Behavior and Gene Expression in a Rat Model of Neuropathic Pain. *Neuromodulation* 2020;23(1):26-35. doi:10.1111/ner.12964
89. Caylor J, Reddy R, Yin S, Cui C, Huang M, Huang C, et al. Spinal cord stimulation in chronic pain: evidence and theory for mechanisms of action. *Bioelectron Med* 2019;5(1):1-41. doi:10.1186/s42234-019-0023-1
90. Rattay F. The basic mechanism for the electrical stimulation of the nervous system. *Neuroscience* 1999;89(2):335-346. doi:10.1016/S0306-4522(98)00330-3
91. Huang L-YM, Gu Y, Chen Y. Communication between neuronal somata and satellite glial cells in sensory ganglia. *Glia* 2013;61:1571-1581. doi:10.1002/glia.22541
92. Abdo H, Calvo-Enrique L, Lopez JM, Song J, Zhang M-D, Usoskin D, et al. Specialized cutaneous Schwann cells initiate pain sensation. *Science* 2019;365:695-699. doi:10.1126/science.aax6452
93. Costa FAL, Neto FLM. Satellite glial cells in sensory ganglia: Its role in pain. *Brazilian J Anesthesiol (English Ed* 2015;65(1):73-81. doi:10.1016/j.bjane.2013.07.013
94. Zhou LJ, Peng J, Xu Y-N, Zeng W-J, Zhang J, Wei X, et al. Microglia are indispensable for synaptic plasticity in the spinal dorsal horn and chronic pain. *Cell Rep* 2019;27:3844-3859.e6. doi:10.1016/j.celrep.2019.05.087
95. Bean BP. The action potential in mammalian central neurons. *Nat Rev Neurosci* 2007;8(6):451-465. doi:10.1038/nrn2148
96. North RY, Li Y, Ray P, Rhines LD, Tatsui CE, Rao G, et al. Electrophysiological and transcriptomic correlates of neuropathic pain in human dorsal root ganglion neurons. *Brain* 2019:1-12. doi:10.1093/BRAIN/AWZ063

97. Huxley AF, Stämpfli R. Direct determination of membrane resting potential and action potential in single myelinated nerve fibres. *J Physiol* 1951;112(3-4):476-495.

98. Harper AA, Lawson SN. Electrical properties of rat dorsal root ganglion neurones with different peripheral nerve conduction velocities. *J Physiol* 1985;359(1):47-63. doi:10.1113/jphysiol.1985.sp015574

99. Villière V, McLachlan EM. Electrophysiological properties of neurons in intact rat dorsal root ganglia classified by conduction velocity and action potential duration. *J Neurophysiol* 1996;76(3):1924-1941.

100. Howells J, Trevillion L, Bostock H, Burke D. The voltage dependence of Ih in human myelinated axons. *J Physiol* 2012;590(7):1625-1640. doi:10.1113/jphysiol.2011.225573

101. Sundt D, Gamper N, Jaffe DB. Spike propagation through the dorsal root ganglia in an unmyelinated sensory neuron: A modeling study. *J Neurophysiol* 2015;114(6):3140-3153. doi:10.1152/jn.00226.2015

102. Amir R, Devor M. Electrical excitability of the soma of sensory neurons is required for spike invasion of the soma, but not for through-conduction. *Biophys J* 2003;84(4):2181-2191. doi:10.1016/S0006-3495(03)75024-3

103. Ito M, Takahashi I. Impulse conduction through spinal ganglion. In: *Electrical Activity of Single Cells*. ; 1960:159-179.

Figure legends

Figure 1: Finite element model (FEM) of a human L5 DRG and surrounding anatomy. a. Representative schematic of the human L5 spinal column, dorsal root ganglion, surrounding anatomy, and a four-contact DRGS electrode lead. The dashed box represents the general area represented by the FEM. b. Exploded view of the concentric cylindrical domains used to create the FEM. On the four-contact DRGS electrode lead, the red contact indicates the active contact, the blue contact is the return contact, and the black contacts are inactive.

Figure 2: DRGS stimulation configurations. Isopotential lines of the voltage distributions generated by DRGS using example stimulation configurations: a. adjacent bipole with the active contact centered above the ganglion, b. adjacent bipole with the active and return contacts straddling the ganglion, c. separated bipole, and d. guarded cathode with the active contact centered above the ganglion. Red contacts are active contacts, blue contacts are return contacts, black contacts are inactive.

Figure 3: Multi-compartment models of DRG sensory neurons. We implemented models of five types of sensory neurons found in DRG: (a) a large-diameter, myelinated Aα- and Aβ-neurons; (b) a small-diameter, thinly-myelinated Aδ-LTMR; (c) a small-diameter, thinly-myelinated Aδ-HTMR; and (d) a small-diameter, nonmyelinated C-nociceptor. The Aα-neuron, Aβ-LTMR, and Aδ-LTMR putatively convey innocuous sensory information, while the Aδ-HTMR and C-nociceptor are putatively nociceptive. For

each cell model, the equivalent circuit diagrams show the active voltage-gated ion channels included in each cell type and a linear leak conductance. Inset action potentials represent the somatic membrane response to a brief intracellular current pulse applied to the peripheral axon.

Figure 4: Simulating the neural response to DRGS. a. Isopotential lines of the voltage distribution generated by bipolar DRGS. The black trace in the DRG represents an example cell trajectory for a pseudounipolar primary sensory neuron. The red contact is the active contact, the blue contact is the return contact, and black contacts are inactive. b. Simulating the time-varying membrane potential of each sensory neuron cell type in response to a 1 mA anodic-first DRGS stimulus train (top trace, gray). The four black traces represent the somatic membrane potential of each type of sensory neuron with the example trajectory shown in part (a). Note that the putatively innocuous neurons (the Aα-neuron, Aβ-LTMR, and Aδ-LTMR) fire action potentials in response to a clinical DRGS pulse, while the putatively nociceptive models (the Aδ-HTMR and C-nociceptor) do not.

Figure 5: Effect of electrode position on neural activation during DRGS. Each plot shows the percentage of each neuron type that generated action potentials in response to DRGS with a pulse width of 300 μs and an amplitude 2 mA or less (i.e. clinical DRGS), as the distance between the electrode lead and the ganglion increased. We examined the effects of electrode position relative to the ganglion for several electrode positions and stimulus polarities: the active (red) contact centered above the ganglion (a, c), the active and return (blue) contacts straddling the ganglion (b, d), anodic-first DRGS (a, b), and cathodic-first DRGS (c, d).

Figure 6: Effect of pulse width on neural activation during DRGS. Each plot shows the percentage of each neuron type that generated action potentials in response to DRGS with a pulse width between 100 μs and 1000 μs, and an amplitude 2 mA or less. We examined the effects of pulse width on neural activation for several electrode positions and stimulus polarities: the active (red) contact centered above the ganglion (a, c), the active and return (blue) contacts straddling the ganglion (b, d), anodic-first DRGS (a, b), and cathodic-first DRGS (c, d).

Figure 7: Effect of pulse frequency on different Aβ-LTMR compartment response frequencies during DRGS. Each plot shows the average response frequency (i.e. the frequency of action potential generation in response to DRGS) of Aβ-LTMR somata (blue), stem axons (orange), centrally-projecting axons (green), and peripherally projecting axons (red). The black lines indicate unity (i.e. the neural compartment is responding in a one-to-one fashion with the stimulus train). We examined the effects of pulse frequency for several electrode positions and stimulus polarities: the active (red) contact centered above the ganglion (a, c), the active and return contacts straddling the ganglion (b, d), anodic-first DRGS (a, b), and cathodic-first DRGS (c, d). Note: some data are not visible due to many compartments having the

same response frequency.

Figure 8: Effect of bipole configuration on neural activation during DRGS. Each plot shows the percentage of modeled Aβ-LTMRs activated by different bipolar DRGS configurations. For each pair of bars, the black and gray bars indicate the percentage of Aβ-LTMRs activated by anodic-first and cathodic-first DRGS, respectively. For the schematics above each pair of bars, the red, blue, and black contacts indicate the active, return, and inactive contacts, respectively. Left-most schematics indicate spinal and peripheral nerve roots. a. Percentage of modeled Aβ-LTMRs activated by adjacent bipoles. b. Percentage of modeled Aβ-LTMRs activated by bipoles with one or more inactive contacts separating the active and return contacts.

Figure 9: Effect of guarded active contact configurations on neural activation during DRGS. For each pair of bars, the black and gray bars indicate the percentage of Aβ-LTMRs activated by anodic-first and cathodic-first DRGS, respectively. For the schematics above each pair of bars, the red, blue, and black contacts indicate the active, return, and inactive contacts, respectively. Left-most schematic indicates spinal and peripheral nerve roots.

Tables

Table 1: Dimensions of the finite element model of a human L5 DRG.

Parameter	Value	Reference
DRG length	9.4 mm	(27)
DRG width	5.9 mm	(27)
Nerve root radius	1.19 mm	(28)
Dural sheath thickness	150 μm	(29)
Foramen height	17.1 mm	(27)
Encapsulation layer	300 μm	(33)
Electrode contact length	1.25 mm	(30)
Electrode radius	0.5 mm	(30)
Electrode contact spacing	5 mm	(30)

Table 2: Electrical conductivities assigned to the anatomical compartments of the finite element model.

Parameter	Value	Reference
Gray matter	0.23 S/m	(31)
White matter (longitudinal)	0.6 S/m	(31)
White matter (transverse)	0.083 S/m	(31)
Dural covering	0.6 S/m	(19)

Bone	0.02 S/m	(32)
General tissue	0.25 S/m	(31)
Encapsulation	0.17 S/m	(33)

Table 3: Validation metrics for the Aα-neuron model. *Indicates a model value outside of the previously-reported experimental ranges.

Aα-fiber			
Parameter	**Our Value**	**Literature Ranges**	**Reference**
Soma AP Amplitude (mV)	108.6	109.72 +/- 11.21	(97)
AP duration (base) (ms)	1.075	0.98 +/- 0.2	(98)
Rise time (ms)*	0.675	0.46 +/- 0.13	(38)
Fall time (ms)*	0.4	0.89 +/- 0.41	(38)
AHP amplitude (mV)	3.68	6.5 +/- 4.2	(51)
AHP half-amplitude duration (ms)	12.175	10.9 +/- 11.0	(99)
Resting potential (mV)	-79.2	-80.0	(100)
Conduction velocity (16.0 μm peripheral axon) (m/s)	90.4	89.7 +/- 7.6	(20)
Conduction velocity (15.0 μm central axon) (m/s)	83.5	89.7 +/- 7.6	(20)

Table 4: Morphological parameters for both Aδ-neuron models.

Parameter	**Value**	**Reference**
Fiber diameter (peripheral)	3.0 μm	(43)
Fiber diameter (central)	2.0 μm	(43)
Fiber diameter (stem)	3.0 μm	(43, 101)
Stem axon length	840 μm	(101–103)
Soma length	29 μm	(43)
Soma diameter	34 μm	(43)
Node length	1.0 μm	(44)
Paranode length	3.0 μm	(44)
Juxtaparanode length	Variable	(44)
Internode length	Variable	(44, 102)

Table 5: Validation metrics for the Aδ-neuron models. *Indicates a model value outside of the previously-reported experimental ranges.

Low threshold mechanoreceptor (LTMR)

Parameter	Model value	Literature ranges	Reference
Soma AP amplitude (mV)	95.6	98.0 +/- 4.0	(51)
AP duration (base) (ms)	1.9	1.76 +/- 0.28	(38)
Rise time (ms)	0.9*	0.68 +/- 0.094	(38)
Fall time (ms)	1.0	1.07 +/- 0.22	(38)
AHP amplitude (mV)	7.9	9.5 +/- 3.7	(52)
AHP half-amplitude duration (ms)	1.6	3.0 +/- 2.6	(52)
Resting potential (mV)	-53.6	-55.2 +/- 9.6	(52)
Conduction velocity (peripheral axon) (m/s)	5.3	1.3 – 12	(52)
Conduction velocity (central axon) (m/s)	2.5	1.3 – 12	(52)
High threshold mechanoreceptor (HTMR)			
Parameter	**Model value**	**Literature ranges**	**Reference**
Soma AP amplitude (mV)	85.9	77.0 +/- 13.2	(52)
AP duration (base) (ms)	3.7	3.0 +/- 0.72	(38)
Rise time (ms)	1.85*	1.18 +/- 0.31	(38)
Fall time (ms)	1.8	1.9 +/- 0.6	(38)
AHP amplitude (mV)	10.0	12.3 +/- 4.1	(52)
AHP half-amplitude duration (ms)	2.0	9.2 +/- 9.0	(52)
Resting potential (mV)	-55.1	54.1 +/- 10.1	(52)
Conduction velocity (peripheral axon) (m/s)	3.7	1.3 – 12	(52)
Conduction velocity (central axon) (m/s)	1.7	1.3 – 12	(52)